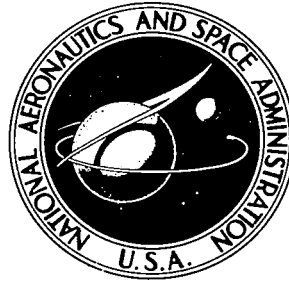


NASA TECHNICAL NOTE



NASA TN D-5251

c. 1

LOAN COPY: RET
AFWL (W/II)
KIRTLAND AFB,



NASA TN D-5251

HEAT TRANSFER TO THE WINDWARD SIDE
OF A FINENESS-RATIO-2.9 CYLINDER
WITH NEARLY SPHERICAL ENDS AT
A MACH NUMBER OF 6 AND ANGLES
OF ATTACK OF 50° , 70° , AND 90°

by James L. Hunt

Langley Research Center

Langley Station, Hampton, Va.



HEAT TRANSFER TO THE WINDWARD SIDE
OF A FINENESS-RATIO-2.9 CYLINDER WITH NEARLY
SPHERICAL ENDS AT A MACH NUMBER OF 6 AND
ANGLES OF ATTACK OF 50° , 70° , AND 90°

By James L. Hunt

Langley Research Center
Langley Station, Hampton, Va.

NATIONAL AERONAUTICS AND SPACE ADMINISTRATION

For sale by the Clearinghouse for Federal Scientific and Technical Information
Springfield, Virginia 22151 - CFSTI price \$3.00

HEAT TRANSFER TO THE WINDWARD SIDE
OF A FINENESS-RATIO-2.9 CYLINDER WITH NEARLY
SPHERICAL ENDS AT A MACH NUMBER OF 6 AND
ANGLES OF ATTACK OF 50°, 70°, AND 90°

By James L. Hunt
Langley Research Center

SUMMARY

An investigation was conducted in the Langley 20-inch Mach 6 tunnel to define the heat transfer to a fineness-ratio-2.9 cylinder with nearly spherical ends ($\frac{1}{4}$ -scale model of the graphite lunar module fuel cask (GLFC)). Heat-transfer data and schlieren photographs were obtained at a nominal Reynolds number, based on model diameter, of 1×10^6 at sweep angles of 0°, 20°, and 40°.

Beckwith's laminar swept infinite-cylinder theory, small-cross-flow theory, and local similarity theory with Libby's three-dimensional stagnation-point theory were used piecewise to predict the laminar heat transfer with acceptable accuracy. Local flat-plate approximations for turbulent heat transfer, calculated by the method of Spalding and Chi, agreed with the data obtained in the turbulent flow regions.

INTRODUCTION

An investigation was conducted in the Langley 20-inch Mach 6 tunnel to define the heat transfer to a fineness-ratio-2.9 cylinder with nearly spherical ends. The configuration is a $\frac{1}{4}$ -scale model of the graphite lunar module fuel cask (GLFC), the heat-shield cask for the radioisotope fuel capsule of the SNAP-27 power system (ref. 1). A major unknown at the time of this investigation was the effect of the nearly spherical ends on the heat-transfer distribution along the cylinder at large angles of attack (flow nearly normal to cylinder). The accurate prediction of heating distribution and level is important because of safety problems concerning the possible reentry of the cask from aborted Apollo missions. Should an abort occur, the GLFC must be capable of returning the nuclear fuel capsule to the earth intact (ref. 2).

The phase-change coating technique, which was developed at the Langley Research Center for determining aerodynamic heat-transfer data on complex configurations, was utilized in this investigation. Heat-transfer data and schlieren photographs were obtained

at a nominal Reynolds number, based on model diameter, of 1×10^6 at angles of attack of 50° , 70° , and 90° corresponding to sweep angles of 40° , 20° , and 0° . Heat-transfer predictions from reference 3 for swept infinite cylinders and from reference 4 for three-dimensional small cross flows were compared with the measured heat transfer to the cylindrical section. The three-dimensional stagnation-point theory of reference 5 and the local similarity theory of reference 6 were used for similar comparisons for the windward side of the nearly spherical end. One purpose of this paper is to determine whether reasonable heat-transfer predictions for a low-fineness-ratio cylinder can be obtained from the piecewise application of these theories for simple shapes.

SYMBOLS

c	specific heat of model
D	diameter of cylindrical section of model
h	heat-transfer coefficient
$h_{IC,\Lambda}$	stagnation-line heat-transfer coefficient of an infinite cylinder at angle of sweep
h_{3D}	three-dimensional stagnation-point heat-transfer coefficient
k	thermal conductivity of air
\bar{k}	thermal conductivity of model
M	Mach number
M_N	Mach number normal to cylinder axis
N_{Pr}	Prandtl number
p	pressure
R	free-stream Reynolds number based on cylinder diameter
r	spherical radius

r_b	blending radius (fig. 1)
r_c	radius of cylindrical section (fig. 1)
r_{sp}	radius of nearly spherical end (fig. 1)
$r_{\perp 20}$	radius of curvature perpendicular to plane of blending radius at Newtonian stagnation point ($s/r_c = 1.41$) for 20° sweep
$r_{\perp 40}$	radius of curvature perpendicular to plane of blending radius at Newtonian stagnation point ($s/r_c = 1.008$) for 40° sweep
s	distance along surface of model
T	temperature
t	ratio of wall temperature (temperature at which coating changes phase) to total temperature of stream
Δ	shock standoff distance
ϵ	inverse density ratio, ρ_∞/ρ_2
η	recovery factor, $\frac{T_{aw} - T_e}{T_t - T_e}$
Λ	sweep angle with respect to cylinder axis (see figs. 6, 11, and 14)
μ	viscosity
ρ	density
ρ_w	density of wall material
ϕ	roll angle, measured from windward ray

Subscripts:

aw	adiabatic wall
e	local value external to boundary layer

s	value at stagnation line
t	total conditions
∞	free-stream conditions ahead of bow shock
2	static condition behind shock

TEST METHOD

Heat-transfer coefficients were obtained by using a phase-change coating technique (ref. 7) which has been developed at the Langley Research Center to determine the heat transfer to complex shapes. This technique employs a thin surface coating of material that undergoes a visible phase change at a known temperature. The times required for visible phase changes to occur at various locations on the model are determined from motion pictures. The patterns so obtained represent lines of constant surface temperature. The heat-transfer coefficient at each point along these recorded isotherms can be calculated exactly from the general heat-conduction equations with the measured surface temperature as a boundary condition provided the adiabatic wall temperature at each point is available and the thermophysical properties of the model material are known. An exact solution of the heat-conduction equation for the specific geometry is not always practical; therefore, the local heat-transfer coefficient for the body is determined from the solution for a semi-infinite slab. The results obtained from the semi-infinite-slab assumption are a good approximation to the solution for the actual body geometry when the depth of heat penetration is small compared with pertinent model dimensions. Detailed discussions of the limits of the semi-infinite-slab assumption as affected by heat penetration depth and as affected by model geometry discontinuities are presented in references 7 and 8, respectively.

FACILITY

The test program was conducted in the Langley 20-inch Mach 6 tunnel. This facility, which operates with air as the test medium, is the intermittent type and exhausts to the atmosphere through a diffuser augmented by an air ejector. Tests were conducted at a stagnation pressure and a stagnation temperature of approximately 251.8 N/cm² and 533.5° K, respectively; these conditions give a nominal Reynolds number of 1×10^6 based on model diameter. A detailed description of the tunnel is given in reference 9.

MODELS

Pertinent dimensions of the $\frac{1}{4}$ -scale GLFC model used in this investigation are given in figure 1. This model was made entirely of plastic for which the value of the square root of the product of the thermophysical properties ($\sqrt{\rho_w c \bar{k}}$), which is essential to the heat-transfer technique utilized herein, was $1.31 \times 10^3 \text{ W}\sqrt{\text{sec}}/\text{m}^2\text{-}^\circ\text{K}$ (ref. 8). This value was determined from measurements of the three thermophysical properties at the average model temperature of the present tests. The technique utilizes a grid model for the purpose of locating phase-change patterns. This grid model (fig. 2) is photographed in the exact position occupied by the plastic model during tests in order to provide a superposable grid that is used to locate the phase-change patterns on the test model.

THEORIES USED IN HEAT-TRANSFER ANALYSIS

No well-established analytical method is available for predicting the flow field, and thus the boundary-layer properties, around an arbitrary blunt body at large angles of attack. The usual method is to approximate the actual body piecewise, that is, by segments of bodies of similar shapes, for which analytic solutions are available; however, the accuracy of this piecemeal application of theory needs to be established for each particular problem.

In an attempt to predict the heat transfer to the windward side of the GLFC at large angles of attack, the following theories were employed:

Cylindrical section ($1.41 \leq s/r_c \leq 5.56$)

(1) The laminar infinite-cylinder theory of reference 3 was used in conjunction with a Newtonian pressure distribution on an infinite cylinder. The reference value of $h_{IC, \Lambda=0^\circ}$ (infinite-cylinder stagnation-line heat-transfer coefficient for 0° sweep) was calculated by the following equation from reference 3:

$$h_{IC, \Lambda=0^\circ} = 0.773 \left(\frac{k_\infty}{D} \right) \left(\frac{R \mu_s}{M_\infty \mu_\infty} \right)^{1/2} \left[\frac{T_\infty}{T_s} \frac{p_s}{p_\infty} \left(\frac{p_s}{p_\infty} - 1 \right) \right]^{1/4} \quad (1)$$

which applies only for $N_{Pr} = 0.7$ and $M_{N, \infty} > 1.5$. The reference value of the stagnation-line heat-transfer coefficient at 20° and 40° sweep was also obtained from reference 3 where

$$h_{IC, \Lambda} = h_{IC, \Lambda=0^\circ} (\cos \Lambda)^{1.1} \quad (2)$$

(2) The laminar small-cross-flow theory of reference 4 was employed on a hemisphere-cylinder configuration using a Newtonian stagnation-point pressure and a modified Newtonian pressure distribution. The streamlines used in conjunction with this theory were calculated according to the method of reference 10.

(3) The turbulent infinite-cylinder stagnation-line theory of reference 3 was used to predict the windward-ray heating where turbulent flow appeared to exist.

(4) The method of Spalding and Chi (ref. 11), with local Mach and Reynolds numbers calculated from a modified Newtonian pressure distribution on a hemisphere-cylinder, was utilized to obtain the local flat-plate approximations for turbulent heat transfer. The Reynolds number was based on streamline distance calculated for a hemisphere-cylinder according to reference 10.

Windward nearly spherical end ($0 \leq s/r_c \leq 1.41$)

(1) The three-dimensional stagnation-point theory of reference 5 was used to obtain the stagnation-point heating rate.

(2) The locally similar, blunt-cylinder, cold-wall theory of reference 6 was used to determine the heat-transfer distribution along the windward ray of the nearly spherical end. The Newtonian pressure distribution along the windward ray is independent of the remaining body; therefore, in obtaining the heat-transfer distribution the windward ray was treated as the chord of an infinite two-dimensional body. This treatment neglects the transverse velocity gradients.

RESULTS AND DISCUSSION

Shock Shapes

Schlieren photographs of the flow about the GLFC model at sweep angles of 0° , 20° , and 40° are presented as figure 3. The shock standoff distance Δ/r_c is shown as a function of s/r_c for each of these sweep angles in figure 4.

At 0° sweep (fig. 4(a)), the shock standoff distance along the midportion of the cylindrical section of the model ($2.8 \leq s/r_c \leq 4.1$) is within 10 percent of that given for an infinite cylinder in reference 12. Because the standoff distance is constant along the cylinder, the flow in this region is believed to be essentially two-dimensional. Therefore, the heat-transfer distribution should be similar to that of an infinite cylinder.

At 20° sweep (fig. 4(b)), the shock standoff distance is relatively close to infinite-cylinder standoff distance (ref. 12 with normal Mach number) only for $4.7 \leq s/r_c \leq 5.2$. Near the Newtonian stagnation point ($s/r_c = 1.188$) where the shock is closer to the body, an empirical curve fit

$$\Delta = r(0.76)\epsilon \quad (3)$$

to the theories of references 13, 14, and 15 for a sphere was used in conjunction with r_{sp} (radius of nearly spherical end), $r_{\perp 20}$ (radius of curvature perpendicular to plane of blending radius), and r_b (blending radius) of the GLFC model with the Mach 6 normal-shock density ratio in an attempt to predict the shock standoff distance. These three shock standoff distances (nondimensionalized by r_c) are also shown in figure 4(b). The minimum (stagnation point) shock standoff distance is best predicted by using the radius of the nearly spherical end.

For 40° sweep (fig. 4(c)), the shock standoff distance does not reach a constant level or approach as close to that of an infinite cylinder as do the shock standoff distances for the other two sweep angles. The shock standoff distance at the Newtonian stagnation point ($s/r_c = 1.008$) is very near to that predicted for a sphere (eq. (3)) with a radius equal to the radius of the cylindrical section.

Heat Transfer at $\Lambda = 0^\circ$

The heat-transfer data at $\Lambda = 0^\circ$ are presented in terms of contour sketches and circumferential distributions of the nondimensional heat-transfer-coefficient ratio $h/h_{IC, \Lambda=0^\circ}$ at various cylinder locations s/r_c . Nominal heat-transfer-coefficient contours are presented only because of their pictorial representation of the overall heat transfer to the GLFC; no discussion is given for these contours at $\Lambda = 0^\circ$ or for the contours at $\Lambda = 20^\circ$ and 40° .

Phase-change patterns.- A sample sequence of photographs of the GLFC model taken during the test at $\Lambda = 0^\circ$ and $t = 0.74$ (ratio of temperature at which coating changes phase to total temperature of stream) and showing the phase-change patterns observed at various times is presented in figure 5. The light areas on the model in these figures indicate areas in which the coating phase change has already occurred and represent regions of higher heat-transfer rate. The interface of the light and dark areas are lines of constant temperature along which the heat-transfer coefficient may be computed by the method discussed in the section entitled "Test Method."

The photographs show a distorted view of the surface because of the angle between the camera and model. The camera view and the orientation of the grid model relative to the stream are shown in figure 6.

In figure 7 the isotherms (obtained from the same test as the photographs of fig. 5) for various values of $\frac{h}{h_{IC, \Lambda=0^\circ}}$ at $s/r_c = 3.475$ (center of cylinder) are superimposed on the camera view of the grid model. The grid lines can be identified by referring to figures 2 and 6. Similar isotherms for $t = 0.61$ are superimposed on the grid model in figure 8. If the adiabatic wall temperature were constant along an isotherm, the

heat-transfer-coefficient ratio would also be constant. Since this condition is approximately correct for the isotherms of figures 7 and 8, the value of $h/h_{IC, \Lambda=0^\circ}$ shown may be taken to be the nominal value for the entire isotherm. All data represented by symbols in the rest of the figures are reduced with respect to a local adiabatic wall temperature calculated at each location on the basis of expansion from the total pressure behind a normal shock to a local Newtonian pressure with a recovery factor η of 0.715.

In the discussion and in the summary of results, only comparisons of heat-transfer calculations and data taken from contour sketches and corrected to correspond with local rather than nominal adiabatic wall temperature are used.

Heat-transfer distribution.- The circumferential heat-transfer-coefficient distributions at one value of s/r_c for $t = 0.74$ and at four values of s/r_c for $t = 0.61$ are given in figure 9. The distribution on both sides of the stagnation line is shown in order to give the reader some indication of the accuracy and repeatability of the data. At the center of the cylindrical section of the model ($s/r_c = 3.475$), the data for $t = 0.74$ are slightly higher than those for $t = 0.61$. Whether this difference is a wall-temperature effect or an error due to using two different temperature-sensitive paints or an accumulation of both is not known.

For $t = 0.61$, the heat-transfer data at $s/r_c = 3.475$ agree with the infinite-cylinder theoretical distribution calculated from reference 4 for approximately 50° around the cylinder and, then, the data begin to exceed the theory. The $h/h_{IC, \Lambda=0^\circ}$ distributions at $s/r_c = 2.325$ and 1.875 are progressively lower than the theoretical distribution up to approximately $|\phi| = 50^\circ$ where they approach the theoretical distribution and then exceed it by the same amount as the distribution at $s/r_c = 3.475$. The distribution at $s/r_c = 1.39$ just inside the periphery ($s/r_c = 1.41$) of the nearly spherical end is very similar to the one at $s/r_c = 2.325$, both of which are above the $s/r_c = 1.875$ distribution with a slight increase in heating being indicated in moving from the cylindrical section onto the blending-radius portion of the nearly spherical end.

These observations indicate that for $R \leq 1 \times 10^6$, $t \leq 0.61$, and $\phi \leq 50^\circ$, the heat transfer to the midportion of the cylindrical section ($2.8 \leq s/r_c \leq 4.1$) (see section entitled "Shock Shapes") at $\Lambda = 0^\circ$ can be predicted by laminar infinite-cylinder theory. For the region between the midportion of the cylindrical section and the nearly spherical end ($1.41 \leq s/r_c \leq 2.8$), infinite-cylinder theory gives a conservative estimate by about 10 percent. For $\phi > 50^\circ$ the data are above the laminar theory. This same trend was observed in the data of reference 3 for $\phi \geq 60^\circ$ where the higher heating was attributed partly to the nonisothermal wall temperature. For the present tests, the wall was also nonisothermal.

Heat Transfer at $\Lambda = 20^\circ$ and 40°

The heat-transfer data at $\Lambda = 20^\circ$ and 40° are presented in terms of contour sketches and circumferential distributions of the nondimensional heat-transfer-coefficient ratios $h/h_{IC,\Lambda=20^\circ}$ and $h/h_{IC,\Lambda=40^\circ}$ at various cylinder locations s/r_c . For both these sweep angles the heat-transfer-coefficient ratios are also given in terms of s/r_c distributions along various longitudinal lines.

The heat transfer along the windward ray of the windward side of the nearly spherical end for $\Lambda = 20^\circ$ is given in terms of an s/r_c distribution of the heat-transfer-coefficient ratio h/h_{3D} where h_{3D} is the three-dimensional Newtonian stagnation-point heat-transfer coefficient calculated according to the method of reference 5.

Phase-change patterns at $\Lambda = 20^\circ$.- The phase-change patterns, orientation of model relative to stream, and superimposed nominal heat-transfer-coefficient contours for the GLFC model at $\Lambda = 20^\circ$ and $t = 0.72$ are presented in figures 10, 11, and 12, respectively. For these conditions the cylindrical section of the GLFC was the area of primary concern. The patterns, orientation, and contours for the GLFC model at $\Lambda = 20^\circ$ and $t = 0.75$ with the windward side of the nearly spherical end as the region of interest are shown in figures 13, 14, and 15, respectively. Again, these figures are presented only for the qualitative picture of the overall heat transfer to the GLFC which they display.

Heat-transfer distribution on cylindrical section at $\Lambda = 20^\circ$.- The circumferential heat-transfer-coefficient distributions at three cylinder locations s/r_c for $t = 0.72$ are given in figure 16. The distributions at these three locations are very close to the same level, all of which are considerably higher than that calculated by use of the swept infinite-cylinder laminar theory of reference 3.

The two theoretical heat-transfer distributions shown by dashed lines in figure 16 were obtained from the small-cross-flow theory of Beckwith (ref. 4) as programed by Bushnell and used extensively in reference 16 to predict the heat-transfer distributions on spherically blunted cones at angle of attack. These two distributions are in good agreement with the data for $|\phi| \leq 40^\circ$ and were obtained by applying the small-cross-flow theory to a configuration that was modified slightly from the GLFC model. Bushnell's program restricts bodies to sphere-cones and sphere-cylinders because of the method used to determine the body streamlines (ref. 10). Therefore, 2.54-cm-radius spherical ends rather than the actual nearly spherical ends shown in figure 1 were used with a 2.54-cm-radius cylinder to provide the theoretical model to which a Newtonian stagnation point and modified Newtonian pressure distribution were applied. The tangency point of the spherical end and cylinder on the theoretical model was taken to be the same as that on the actual GLFC model.

The distribution from small-cross-flow theory is not shown in the vicinity of $\phi = 0^\circ$ because of an incorrect theoretical trend in this region. Beckwith (ref. 4) shows that the small-cross-flow theory predicts a heating level near the stagnation line of a yawed cylinder which varies with distance along a streamline in essentially the same way as the variation on a flat plate. He concludes that this variation is incorrect from physical considerations as well as from the exact solution for a swept cylinder and shows that the heating rates predicted in this region by the small-cross-flow theory are low by 10 to 50 percent depending directly on the sweep angle and the wall-to-total temperature ratio.

Starting at $|\phi| = 40^\circ$ the experimental heating becomes increasingly larger than the heating calculated from laminar small-cross-flow theory. To determine whether this increase in heating was caused by transition from laminar to turbulent flow, a turbulent heat-transfer distribution was calculated by the method of Spalding and Chi (ref. 11), applied along the same streamlines used in the calculations with the laminar small-cross-flow theory. The good agreement between this calculation and the data for $|\phi| > 50^\circ$ indicates that the increase in heating may have been caused by transition. Since the data are laminar on the leading edge and may be turbulent for $|\phi| > 50^\circ$, the transition is probably of the type caused by cross-flow instability which is examined extensively in reference 17.

The measured spanwise heat-transfer distribution is shown in figure 17(a) for $\phi = 0^\circ, 15^\circ, \text{ and } 30^\circ$ and in figure 17(b) for $\phi = 45^\circ \text{ and } 60^\circ$. Also shown are distributions obtained from the laminar small-cross-flow theory and turbulent-flow method previously discussed. The small-cross-flow distribution should only be compared with the data for $s/r_c \geq 1.41$ because of the difference in the ends of the theoretical and actual models. For $1.41 \leq s/r_c \leq 4.0$, the heat transfer predicted by this theory at $\phi = 15^\circ$ and 30° is in good agreement with experimental data (fig. 17(a)). The decrease in the theoretical distributions for $s/r_c > 4$ is probably, as indicated in reference 16, due to a breakdown in the streamline calculation procedure rather than due to shortcomings of the small-cross-flow theory. At $\phi = 45^\circ$ (fig. 17(b)) the heat-transfer data appear to be transitional for $s/r_c \geq 1.41$, since they are above the laminar theory and approach the turbulent level (Spalding and Chi) at large values of s/r_c . At $\phi = 60^\circ$, a comparison of the data and calculations indicates that the heating probably is transitional for $1.41 \leq s/r_c \leq 3.6$ and turbulent for $s/r_c \geq 3.6$.

The local Reynolds numbers used in calculating the turbulent heating by the method of Spalding and Chi were based on the distance from the Newtonian stagnation point along the streamlines to which the small-cross-flow theory was applied. This method seems to give good results beyond the point at which the decrease in the laminar heat-transfer theory was believed to be caused by errors in the streamline calculations. Apparently these errors in the streamline calculations do not have any effect on the method of predicting turbulent heat transfer.

Heat-transfer distribution along windward ray of windward nearly spherical end at $\Lambda = 20^\circ$. - The measured heat-transfer distribution on the windward ray of the nearly spherical end at $\Lambda = 20^\circ$ and $t = 0.75$ is shown in figure 18 in terms of h/h_{3D} where h_{3D} is the three-dimensional Newtonian stagnation-point heat-transfer coefficient calculated according to the method of reference 5 using the nearly spherical end blending radius r_b and the radius of curvature perpendicular to the plane of the blending radius at the Newtonian stagnation point r_{120} (see fig. 1(b)). The accuracy in locating the locations s/r_c of the data points (fig. 15) for $1.2 \leq s/r_c \leq 1.6$ leaves much to be desired even with careful study of the original film; nevertheless, the theoretical distribution (solid-line curve) calculated by the method of reference 6 (treating the windward ray as the chord of an infinite cylinder) with the cold-wall approximation and a Newtonian pressure distribution gives good agreement with the data for $0.2 \leq s/r_c \leq 1.45$. Note that peak heating occurs approximately at the Newtonian stagnation point ($s/r_c = 1.188$) and is predicted within 5 percent by the method of Libby (ref. 5). Good agreement with theory for the windward streamline is shown over most of the nearly spherical end.

Phase-change patterns at $\Lambda = 40^\circ$. - The phase-change patterns, orientation of model relative to stream, and superimposed nominal heat-transfer-coefficient contours for the GLFC model at $\Lambda = 40^\circ$ and $t = 0.69$ are presented in figures 19, 20, and 21, respectively.

Heat-transfer distribution at $\Lambda = 40^\circ$. - In figure 22, the circumferential heat-transfer distributions at three spanwise locations s/r_c are compared with those calculated by the infinite-swept-cylinder and small-cross-flow theories of Beckwith (refs. 3 and 4, respectively) and with a turbulent distribution based on the method of Spalding and Chi (ref. 11). Also shown in the figure is the turbulent heating along the stagnation line of an infinite cylinder from reference 3.

Comparison of the heating data along the stagnation line with laminar and turbulent swept-cylinder calculations strongly suggests that the flow is transitional for these conditions. This result would have been expected on the basis of the transition criteria for leading edges void of boundary-layer contamination from adjacent surfaces established by Bushnell in reference 18. For $\phi > 40^\circ$ the heating data approach the predicted turbulent distribution as s/r_c increases, probably because of the change from transitional to fully developed turbulent flow. An orthogonal view of this phenomenon is shown in the s/r_c distributions of figure 23. Here, the experimental distributions at $\phi = 15^\circ, 30^\circ$, and 45° approach calculated turbulent levels at $s/r_c \approx 5.4, 5.1$, and 4.2 , respectively. The local Reynolds numbers (based on the streamlines used in the small-cross-flow theory) at these respective locations are $6.2 \times 10^5, 5.9 \times 10^5$, and 5.0×10^5 . Again the transition is probably of the type caused by cross-flow instability as examined extensively in reference 17.

SUMMARY OF RESULTS

A summary of the results obtained from an investigation of the heat transfer to the windward side of a $\frac{1}{4}$ -scale model of the graphite lunar module fuel cask is presented for a nominal Reynolds number of 1×10^6 , a Mach number of 6, and sweep angles of 0° , 20° , and 40° .

Sweep Angle of 0°

1. For $|\phi| \leq 50^\circ$ (approximate) the heat transfer to the midportion of the cylindrical section ($2.8 \leq s/r_c \leq 4.1$) can be predicted by laminar infinite-cylinder theory.
2. For $|\phi| \geq 50^\circ$ (approximate), the infinite-cylinder laminar theory gives a conservative estimate of the heat transfer to the region between the midportion of the cylindrical section and the nearly spherical end ($1.41 \leq s/r_c \leq 2.8$).
3. A slight increase in heating was observed on a narrow peripheral segment on the blending-radius portion of the nearly spherical end just downstream of the tangency point of the cylinder and nearly spherical end.

Sweep Angle of 20°

Cylindrical section

1. For $15^\circ \leq |\phi| \leq 40^\circ$ (approximate), the heat transfer predicted by laminar small-cross-flow theory is in good agreement with the data.
2. For $40^\circ \leq |\phi| \leq 50^\circ$ (approximate), the heating data are higher than heat transfer calculated from the small-cross-flow theory.
3. For $|\phi| \geq 50^\circ$ (approximate), the heat-transfer data follow a turbulent distribution calculated according to the method of Spalding and Chi.

Windward nearly spherical end

1. Peak heating occurs approximately at the Newtonian stagnation point ($s/r_c = 1.188$) with the peak value being predicted within 5 percent by the three-dimensional method of Libby.
2. For $0.2 \leq s/r_c \leq 1.45$, the laminar, locally similar, blunt-cylinder, cold-wall distribution of Beckwith and Cohen gives acceptable results.

Sweep Angle of 40°

1. The heating on the cylindrical section only is transitional along the stagnation line (bracketed below and above by laminar and turbulent infinite-swept-cylinder theory)

as predicted by the criteria of Bushnell for transition on leading edges void of boundary-layer contamination from adjacent surfaces.

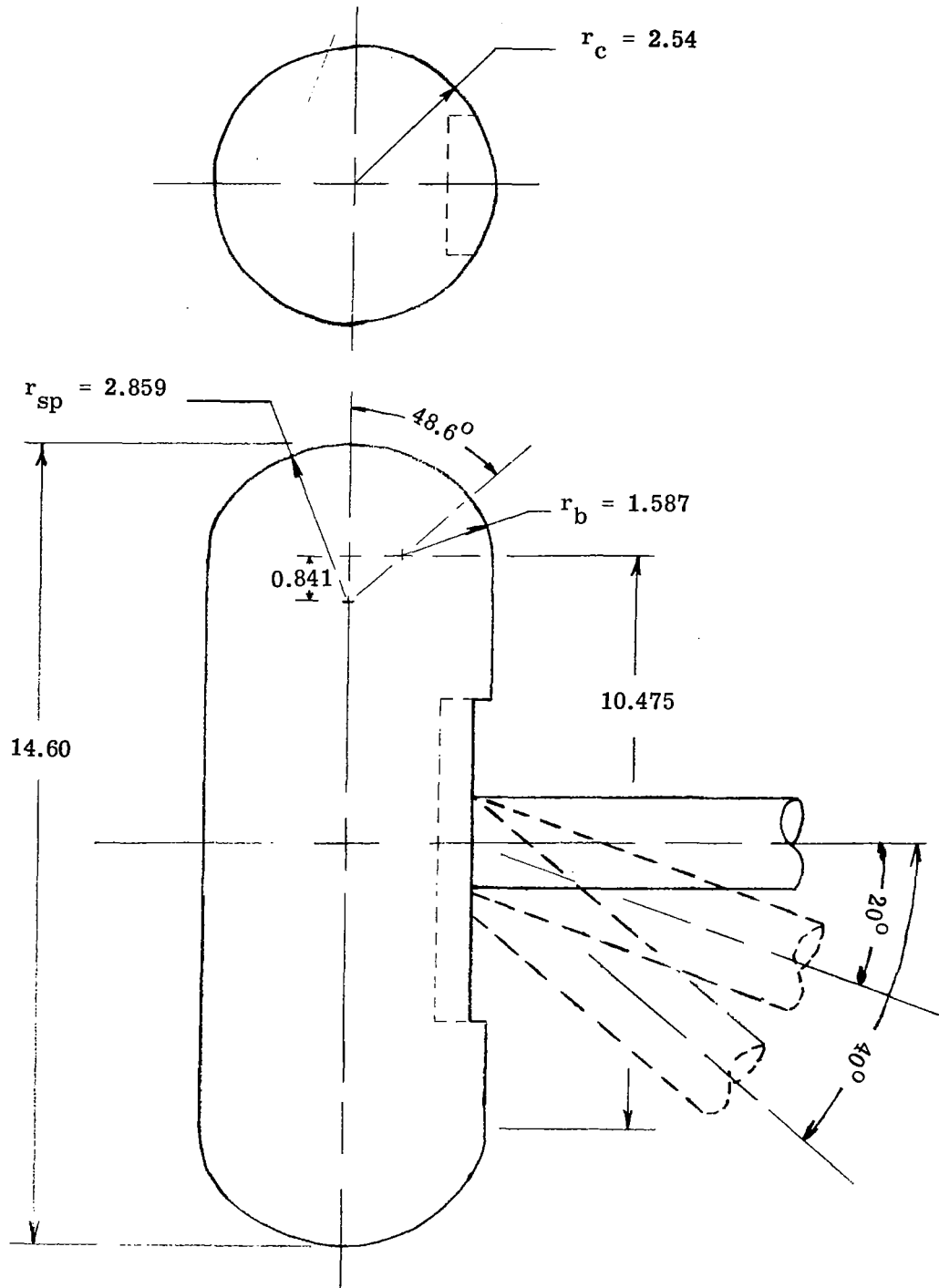
2. For $|\phi| \cong 40^\circ$, as s/r_c increases the heating data approach the turbulent distribution calculated by the method of Spalding and Chi.

Langley Research Center,
National Aeronautics and Space Administration,
Langley Station, Hampton, Va., April 7, 1969,
124-07-02-60-23.

REFERENCES

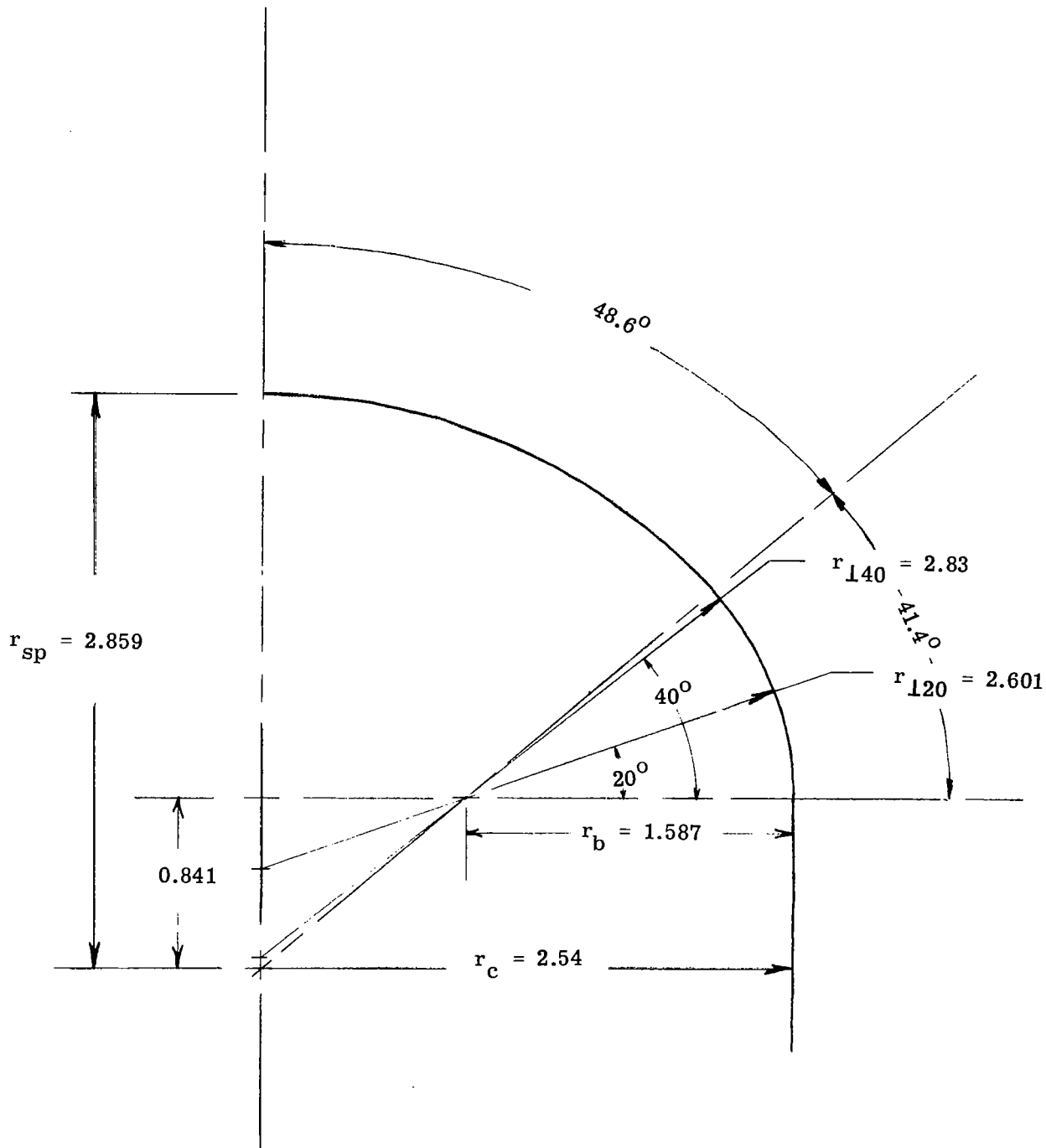
1. Kahn, Stewart F.; and Dohner, Clark V.: Reentry Safety of Isotopic Systems. AIAA Paper No. 68-1166, Dec. 1968.
2. Brunner, M. J.; Dohner, C. V.; and Lawit, R. L.: Re-Entry of Radioactive Power Sources. J. Spacecraft Rockets, vol. 5, no. 4, Apr. 1968, pp. 448-453.
3. Beckwith, Ivan E.; and Gallagher, James J.: Local Heat Transfer and Recovery Temperatures on a Yawed Cylinder at a Mach Number of 4.15 and High Reynolds Numbers. NASA TR R-104, 1961. (Supersedes NASA MEMO 2-27-59L.)
4. Beckwith, Ivan E.: Similarity Solutions for Small Cross Flows in Laminar Compressible Boundary Layers. NASA TR R-107, 1961.
5. Libby, Paul A.: Heat and Mass Transfer at a General Three-Dimensional Stagnation Point. NASA CR-817, 1967.
6. Beckwith, Ivan E.; and Cohen, Nathaniel B.: Application of Similar Solutions to Calculation of Laminar Heat Transfer on Bodies With Yaw and Large Pressure Gradient in High-Speed Flow. NASA TN D-625, 1961.
7. Jones, Robert A.; and Hunt, James L.: Use of Fusible Temperature Indicators for Obtaining Quantitative Aerodynamic Heat-Transfer Data. NASA TR R-230, 1966.
8. Hunt, James L.; and Jones, Robert A.: Effects of Several Ramp-Fairing, Umbilical, and Pad Configurations on Aerodynamic Heating to Apollo Command Module at Mach 8. NASA TM X-1640, 1968.
9. Sterrett, James R.; and Emery, James C.: Extension of Boundary-Layer-Separation Criteria to a Mach Number of 6.5 by Utilizing Flat Plates With Forward-Facing Steps. NASA TN D-618, 1960.
10. Harris, E. L.: Determination of the Streamlines on a Sphere-Cone at Angle of Attack From the Measured Surface Pressure Distribution. NOLTR 63-37, U.S. Navy, Mar. 1963.
11. Spalding, D. B.; and Chi, S. W.: The Drag of a Compressible Turbulent Boundary Layer on a Smooth Flat Plate With and Without Heat Transfer. J. Fluid Mech., vol. 18, pt. 1, Jan. 1964, pp. 117-143.
12. Fuller, Franklyn B.: Numerical Solutions for Supersonic Flow of an Ideal Gas Around Blunt Two-Dimensional Bodies. NASA TN D-791, 1961.
13. Ridyard, Herbert W.; and Storer, Elsie M.: Stagnation-Point Shock Detachment of Blunt Bodies in Supersonic Flow. J. Aerosp. Sci. (Readers' Forum), vol. 29, no. 6, June 1962, pp. 751-752.

14. Van Dyke, Milton D.; and Gordon, Helen D.: Supersonic Flow Past a Family of Blunt Axisymmetric Bodies. NASA TR R-1, 1959.
15. Fink, M. R.; Clark, J. W.; and Miller, D. P.: Approximate Method for Calculating Flow Fields Around Blunt-Nosed Slender Bodies at Hypersonic Speeds. Transactions of the Sixth Symposium on Ballistic Missile and Aerospace Technology, Vol. IV, DCAS-TDR-62-40, U.S. Air Force, Aug. 1961, pp. 423-456. (Available from DDC as AD-329289.)
16. Bushnell, Dennis M.; Jones, Robert A.; and Huffman, Jarrett K.: Heat-Transfer and Pressure Distributions on Spherically Blunted 25° Half-Angle Cone at Mach 8 and Angles of Attack up to 90° . NASA TN D-4792, 1968.
17. Chapman, Gary T.: Some Effects of Leading-Edge Sweep on Boundary-Layer Transition at Supersonic Speeds. NASA TN D-1075, 1961.
18. Bushnell, Dennis M.: Effects of Shock Impingement and Other Factors on Leading-Edge Heat Transfer. NASA TN D-4543, 1968.



(a) Entire model.

Figure 1.- One-quarter-scale model of graphite LM fuel cask (GLFC). All linear dimensions are in centimeters.



(b) Details of intersection of nearly spherical end and cylinder.

Figure 1.- Concluded.

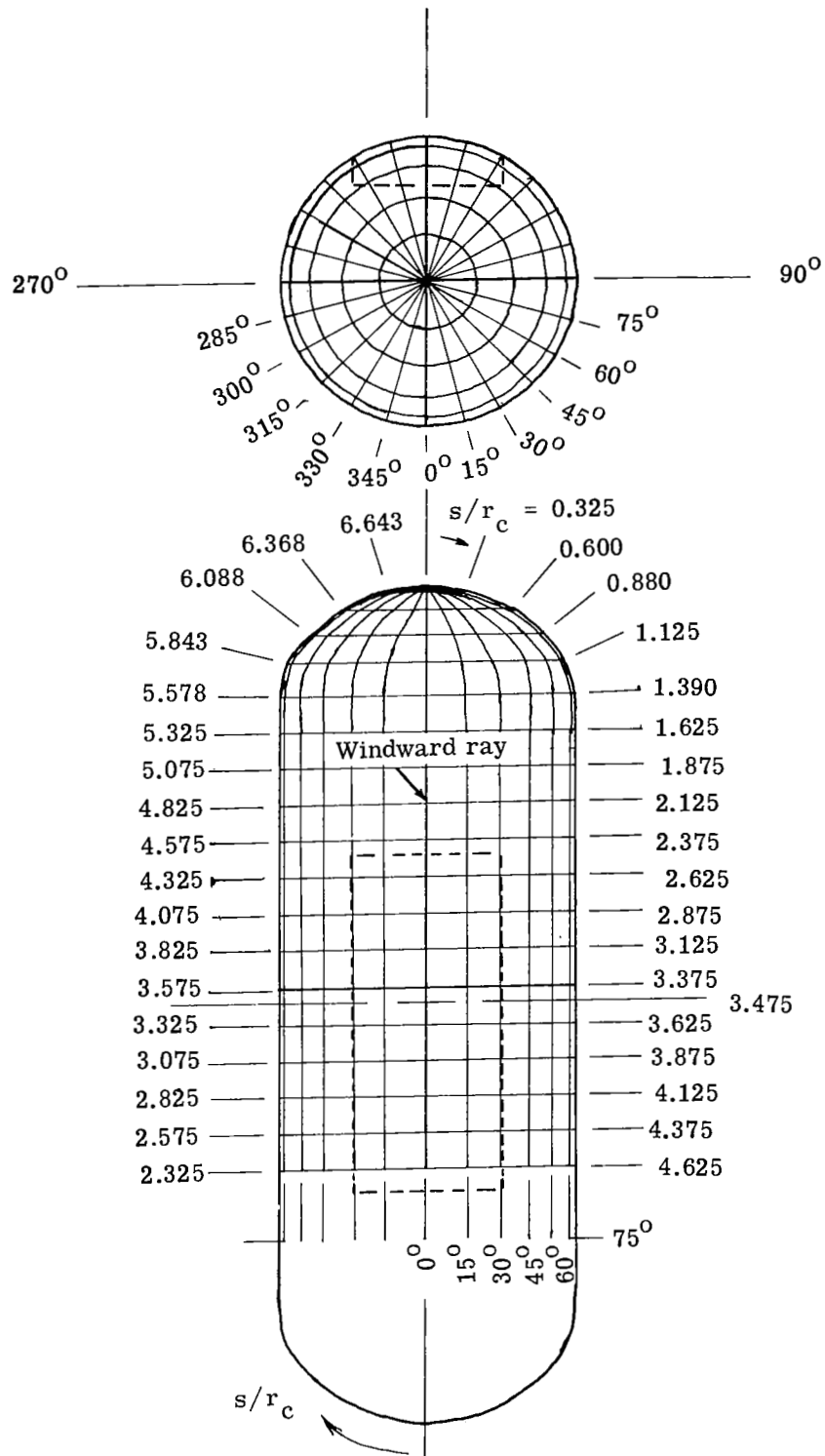
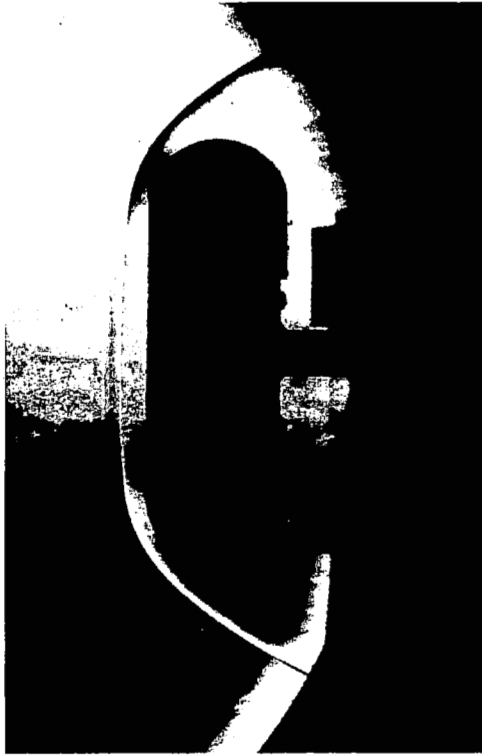


Figure 2.- Grid model.



(a) $\Lambda = 0^\circ$.



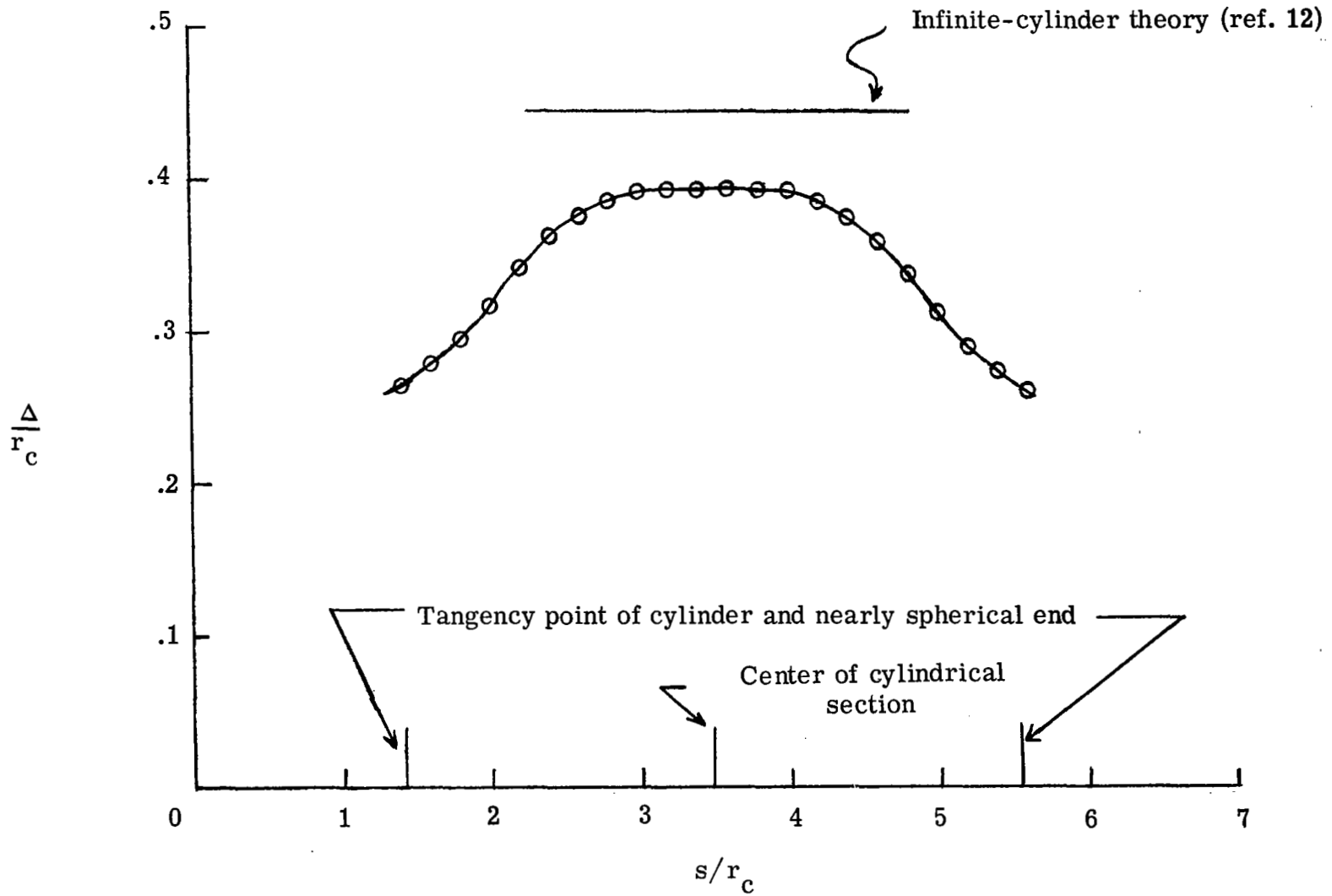
(b) $\Lambda = 20^\circ$.



(c) $\Lambda = 40^\circ$.

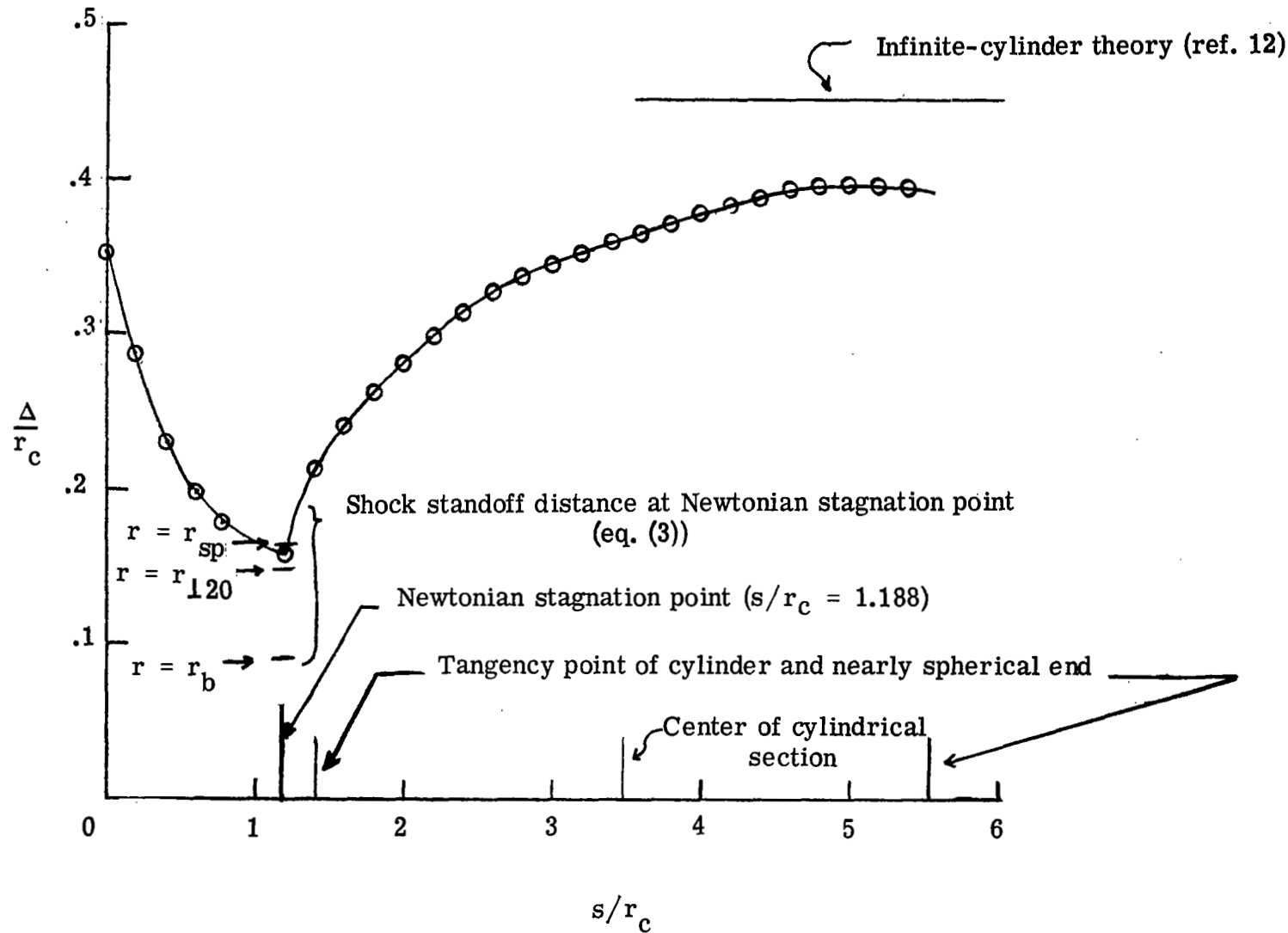
Figure 3.- Schlieren photographs of $\frac{1}{4}$ -scale model of LM fuel cask. $M_\infty = 6.0$.

L-69-1318



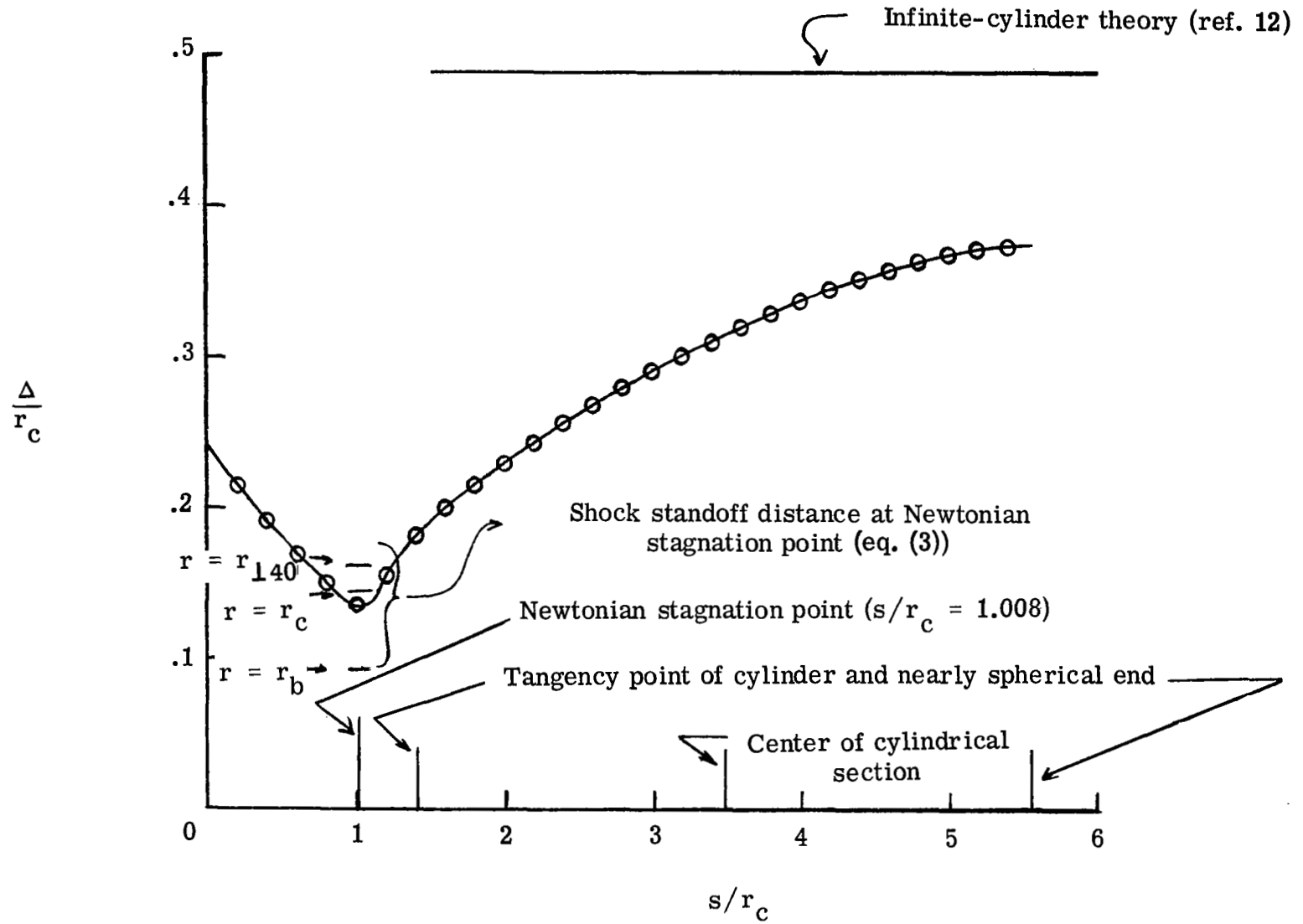
(a) $\Lambda = 0^\circ$.

Figure 4.- Shock-standoff-distance distribution. $M_\infty = 6.0$; $R = 1.0 \times 10^6$.



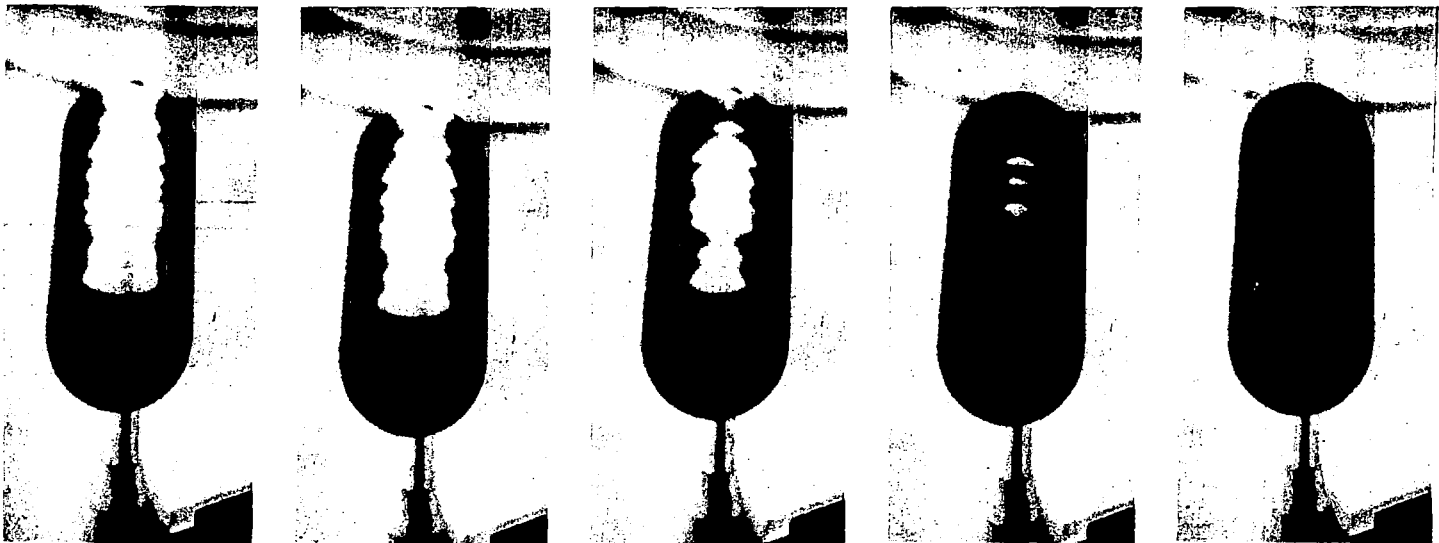
(b) $\Lambda = 20^\circ$.

Figure 4.- Continued.



(c) $\Lambda = 40^\circ$.

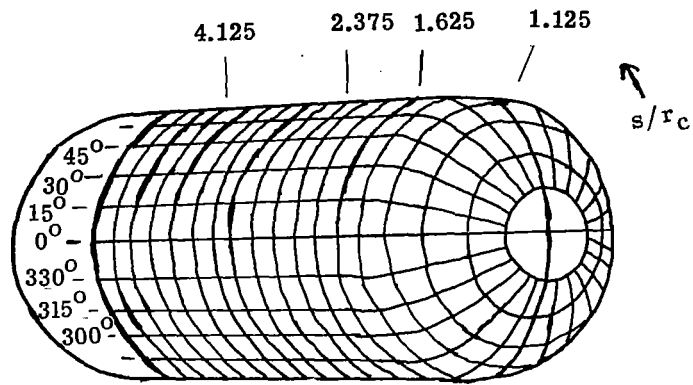
Figure 4.- Concluded.



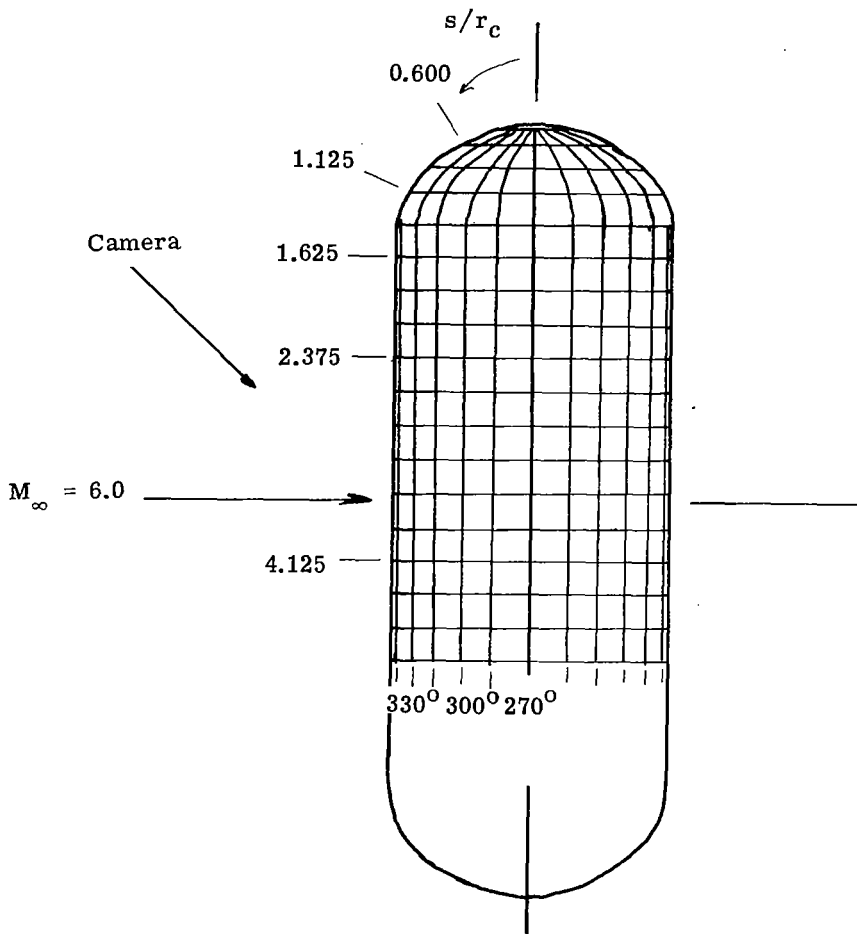
← Increasing time

Figure 5.- Photographs of phase-change patterns at $\Lambda = 0^\circ$.

L-69-1319



(a) Camera view.



(b) Profile view perpendicular to stream.

Figure 6.- Model orientation at $\Lambda = 0^\circ$.

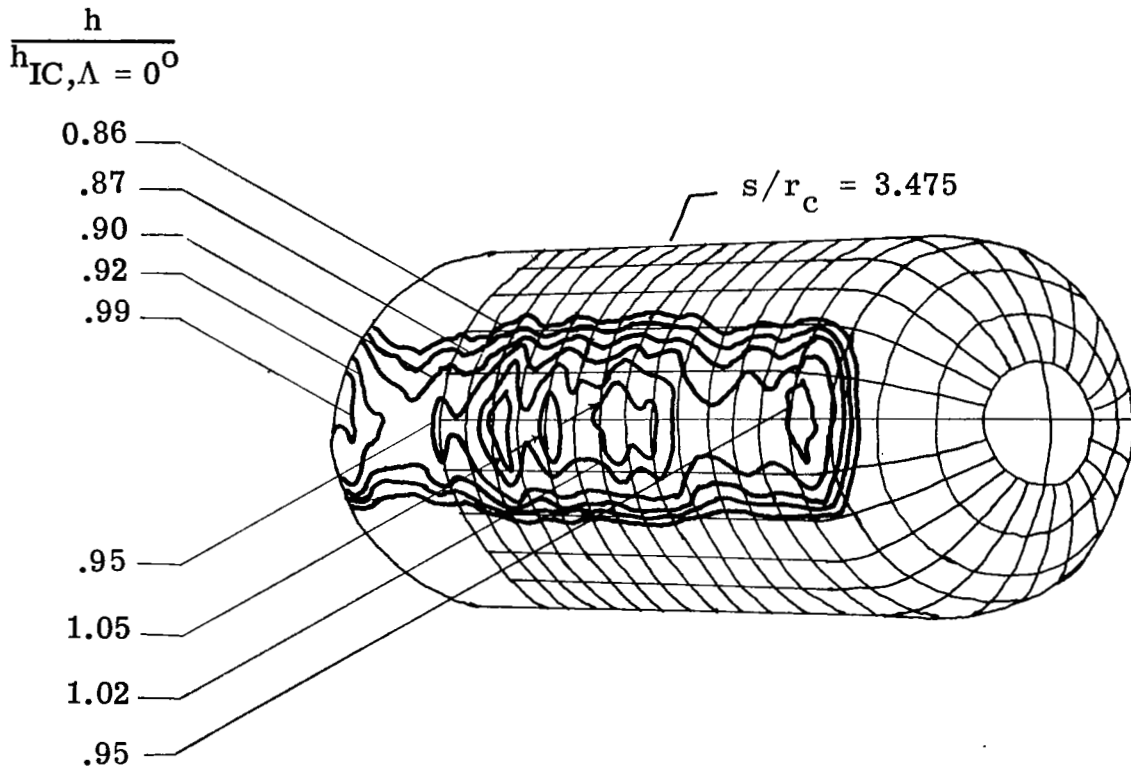


Figure 7.- Nominal heat-transfer-coefficient contours superimposed on camera view of grid model for $\Lambda = 0^\circ$, $t = 0.74$, $R = 0.96 \times 10^6$, and $h_{IC, \Lambda = 0^\circ} = 3.70 \times 10^2 \text{ W/m}^2\text{-}^\circ\text{K}$.

$$\frac{h}{h_{IC, \Lambda = 0^\circ}}$$

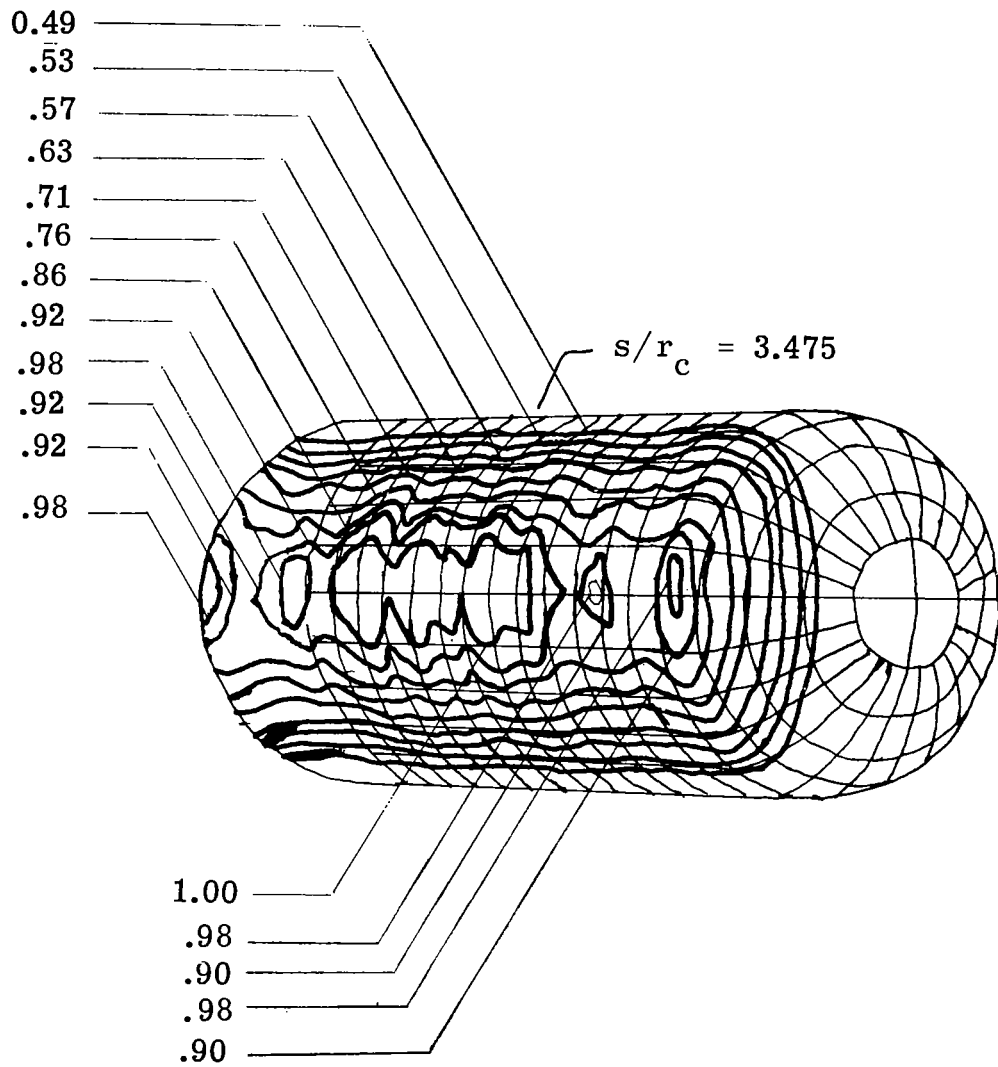


Figure 8.- Nominal heat-transfer-coefficient contours superimposed on camera view of grid model for $\Lambda = 0^\circ$, $t = 0.61$, $R = 0.96 \times 10^6$, and $h_{IC, \Lambda = 0^\circ} = 3.68 \times 10^2 \text{ W/m}^2\text{-}^\circ\text{K}$.

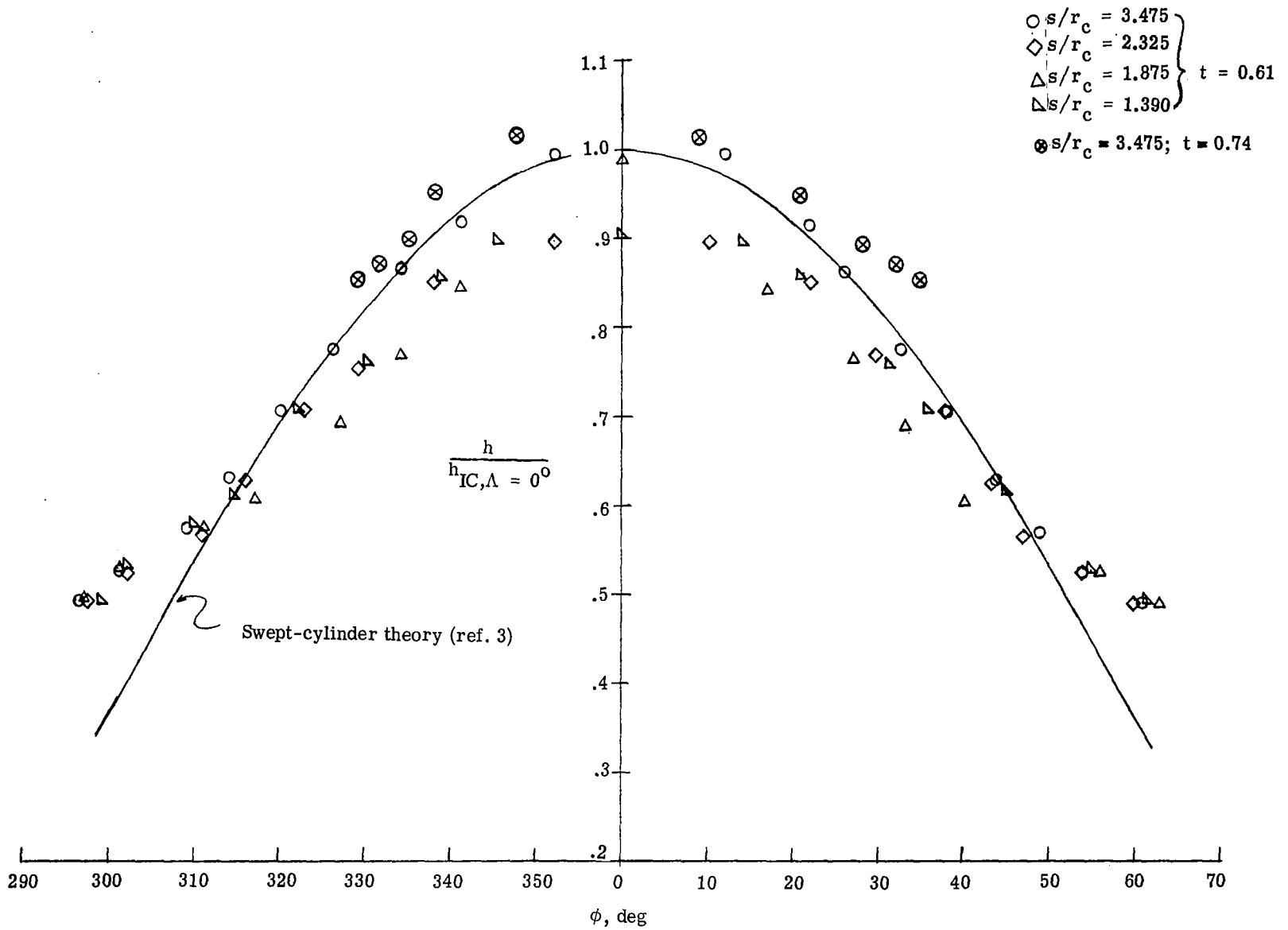
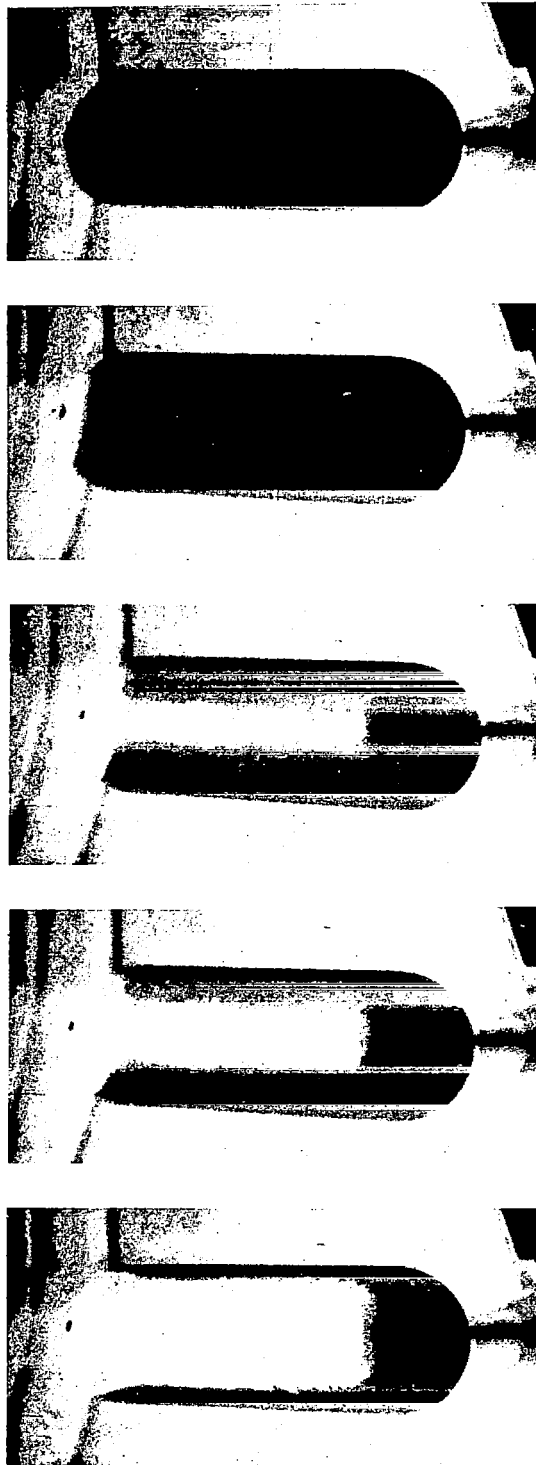
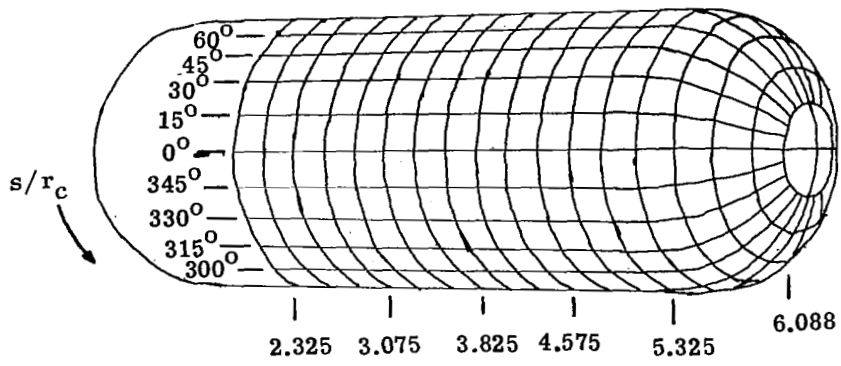


Figure 9.- Circumferential heat-transfer-coefficient distribution for $\Lambda = 0^\circ$, $R = 0.96 \times 10^6$, and $h_{IC, \Lambda = 0^\circ} = 3.70 \times 10^2 \text{ W/m}^2\text{-}^\circ\text{K}$.

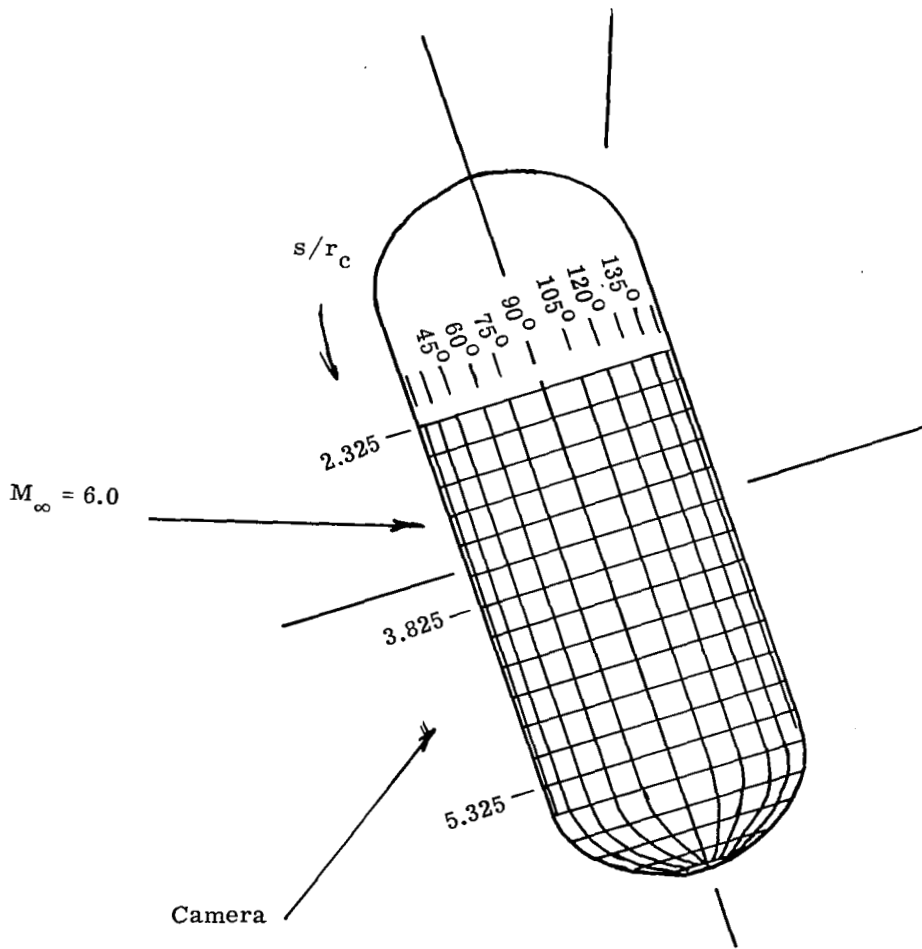


Increasing time

L-69-1320
Figure 10.- Photographs of phase-change patterns at $\Lambda = 20^\circ$.

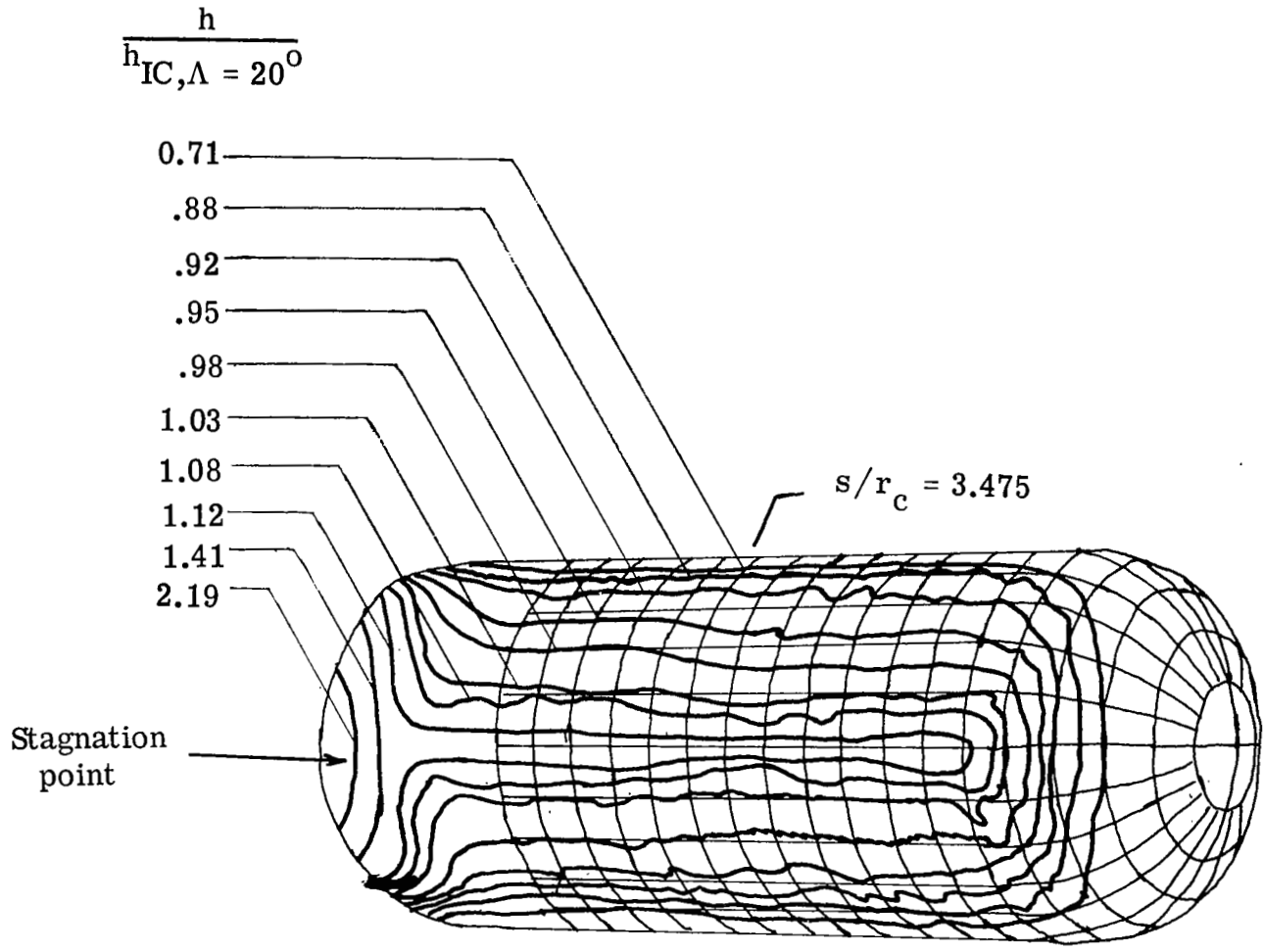


(a) Camera view.



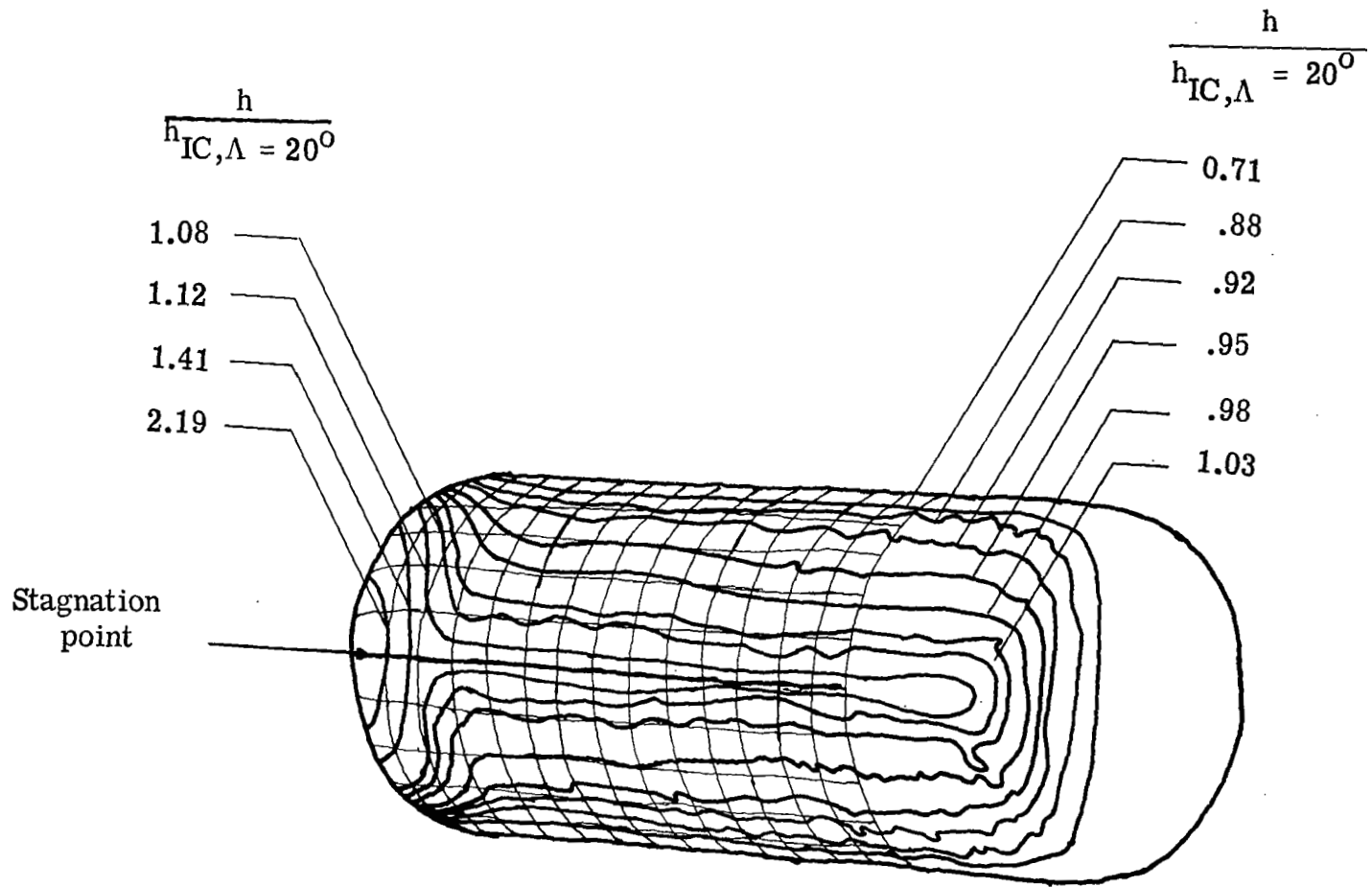
(b) Profile view perpendicular to stream.

Figure 11.- Model orientation at $\Lambda = 20^\circ$.



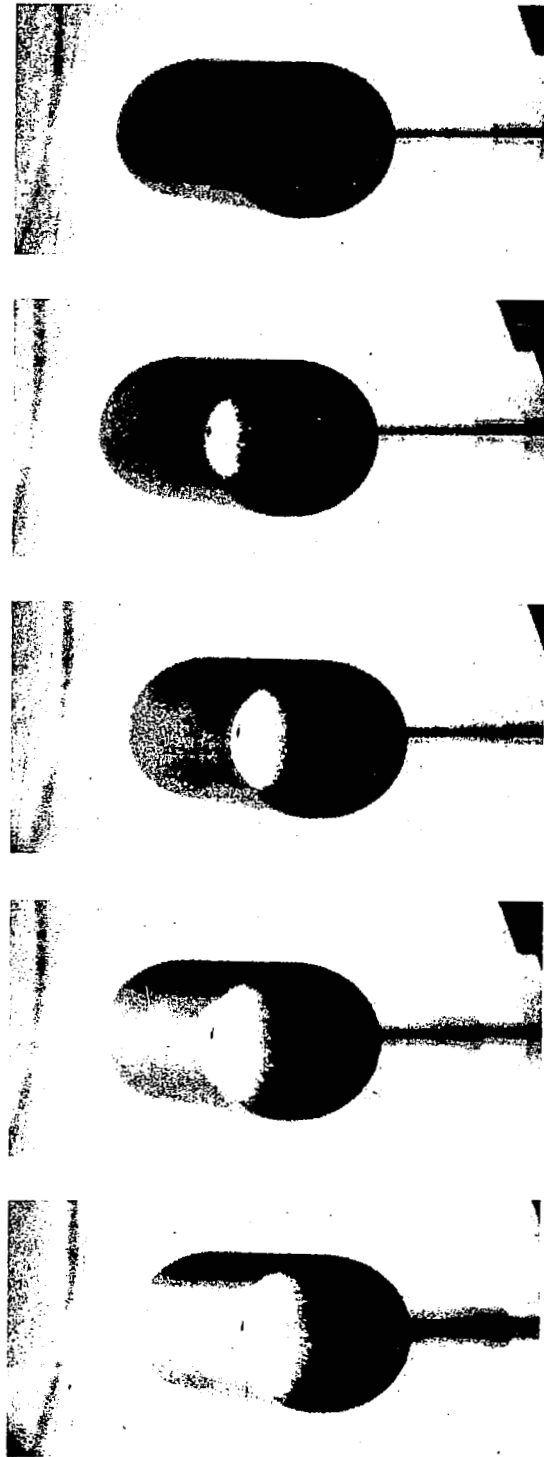
(a) Contours superimposed on camera view of grid model.

Figure 12.- Nominal heat-transfer-coefficient contours for $\Lambda = 20^\circ$, $t = 0.72$, $R = 0.99 \times 10^6$, and $h_{IC, \Lambda = 20^\circ} = 3.49 \times 10^2 \text{ W/m}^2\text{-}^\circ\text{K}$.



(b) Contours superimposed on inversed camera view of grid model.

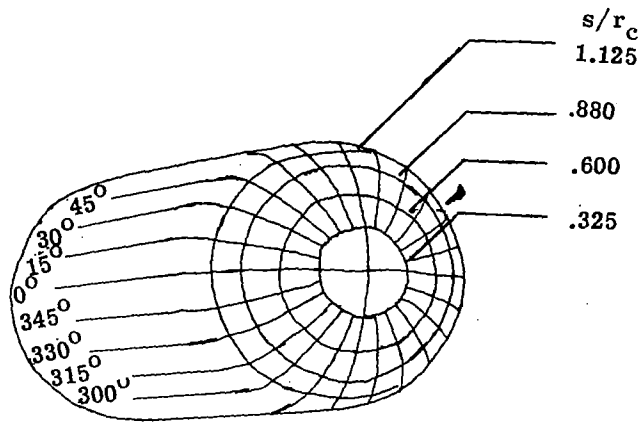
Figure 12.- Concluded.



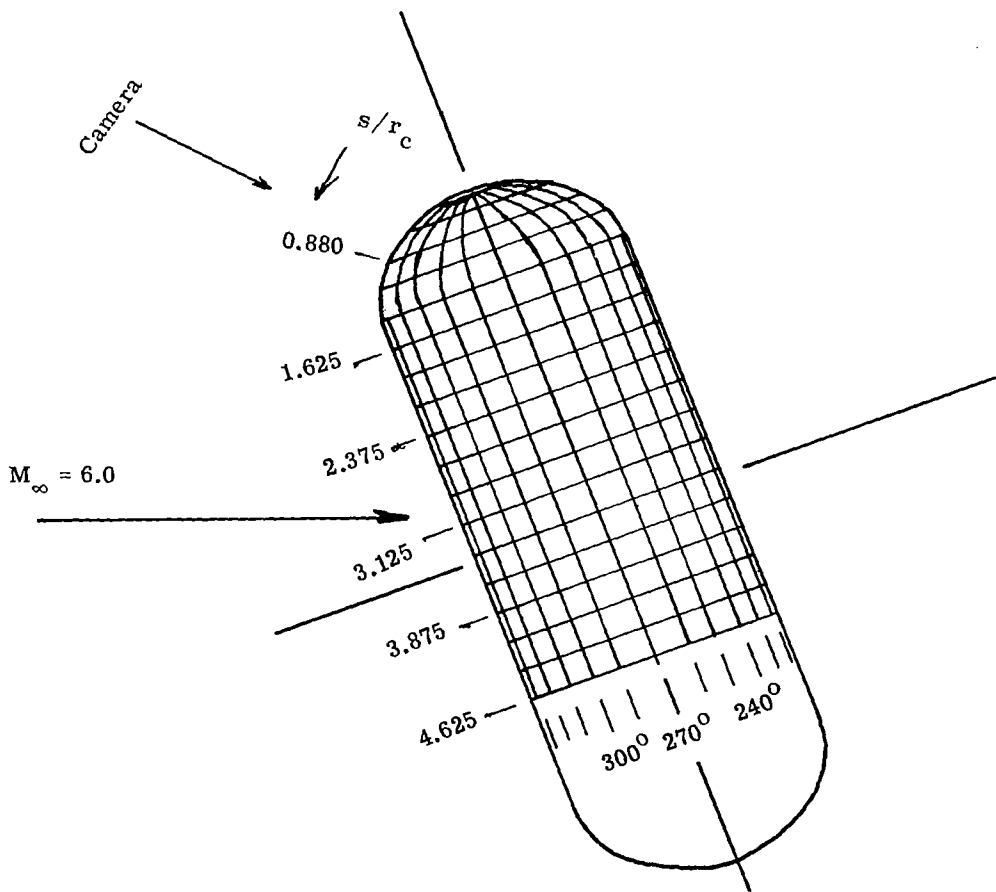
Increasing time

Figure 13.- Photographs of phase-change patterns on windward side of nearly spherical end at $\Lambda = 20^\circ$.

L-69-1321



(a) Camera view.



(b) Profile view perpendicular to stream.

Figure 14.- Orientation of windward side of nearly spherical end at $\Lambda = 20^\circ$.

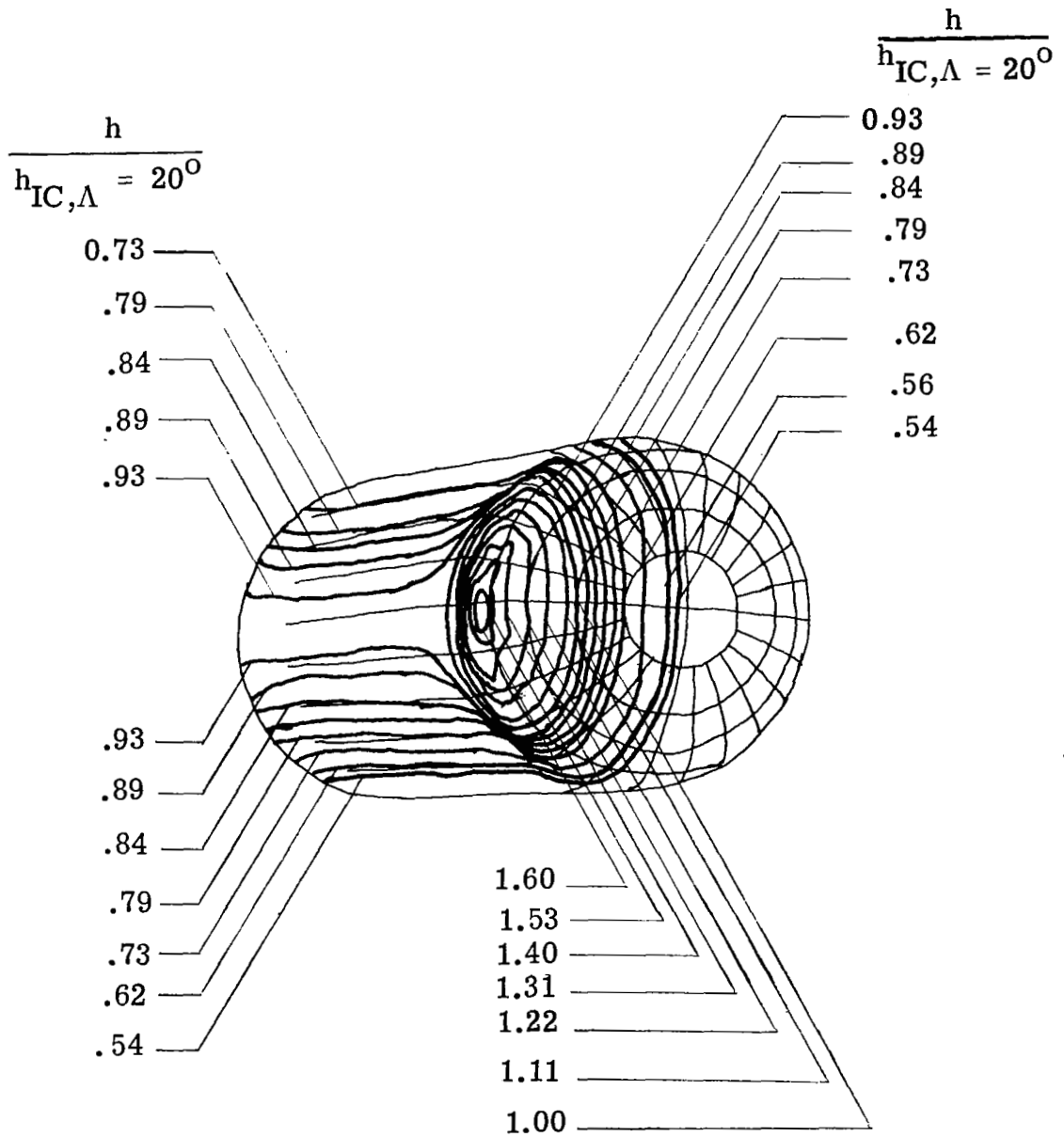


Figure 15.- Nominal heat-transfer-coefficient contours superimposed on camera view of grid model for $\Lambda = 20^\circ$, $t = 0.75$, $R = 0.97 \times 10^6$, and $h_{IC, \Lambda = 20^\circ} = 3.49 \times 10^2 \text{ W/m}^2 \cdot ^\circ\text{K}$.

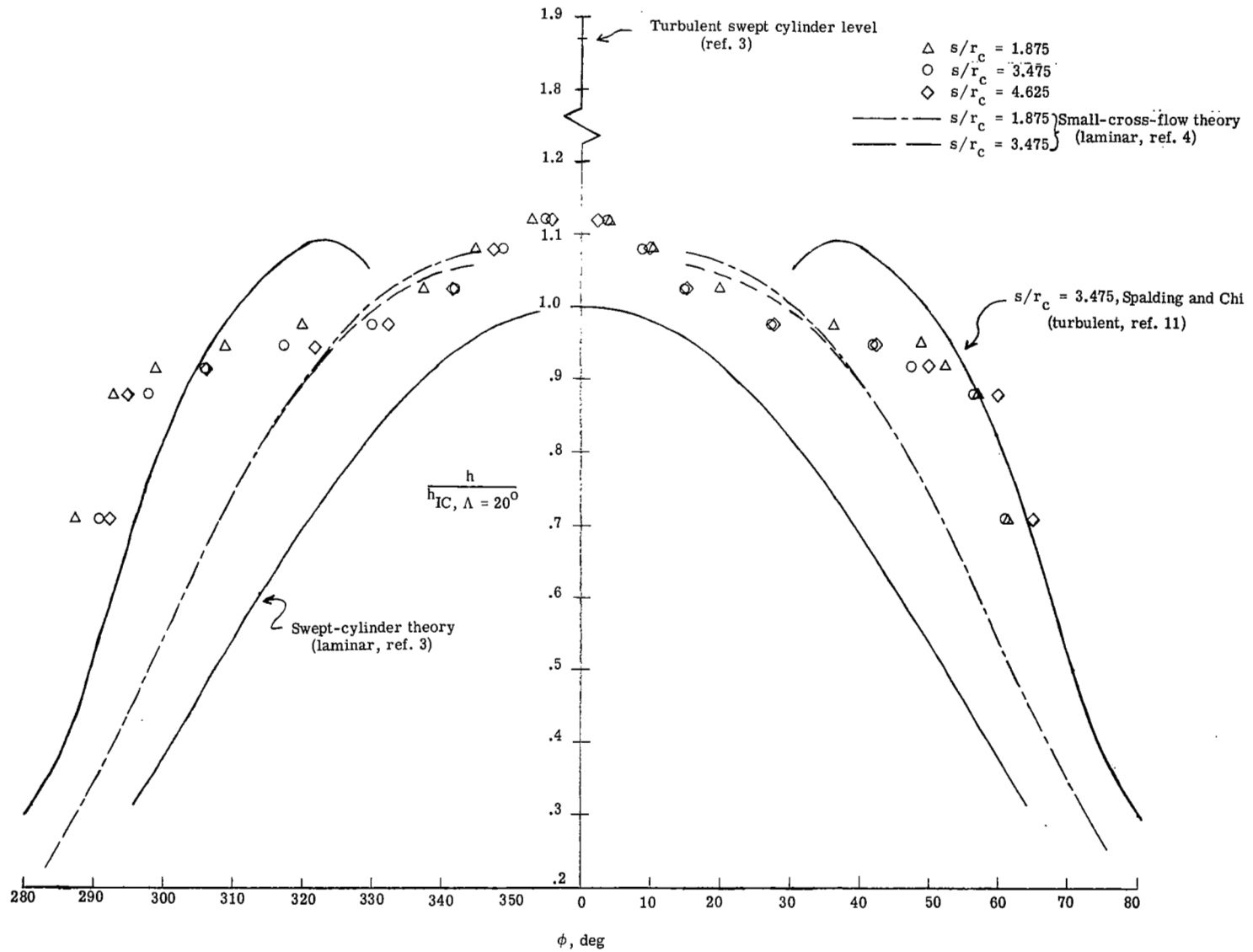
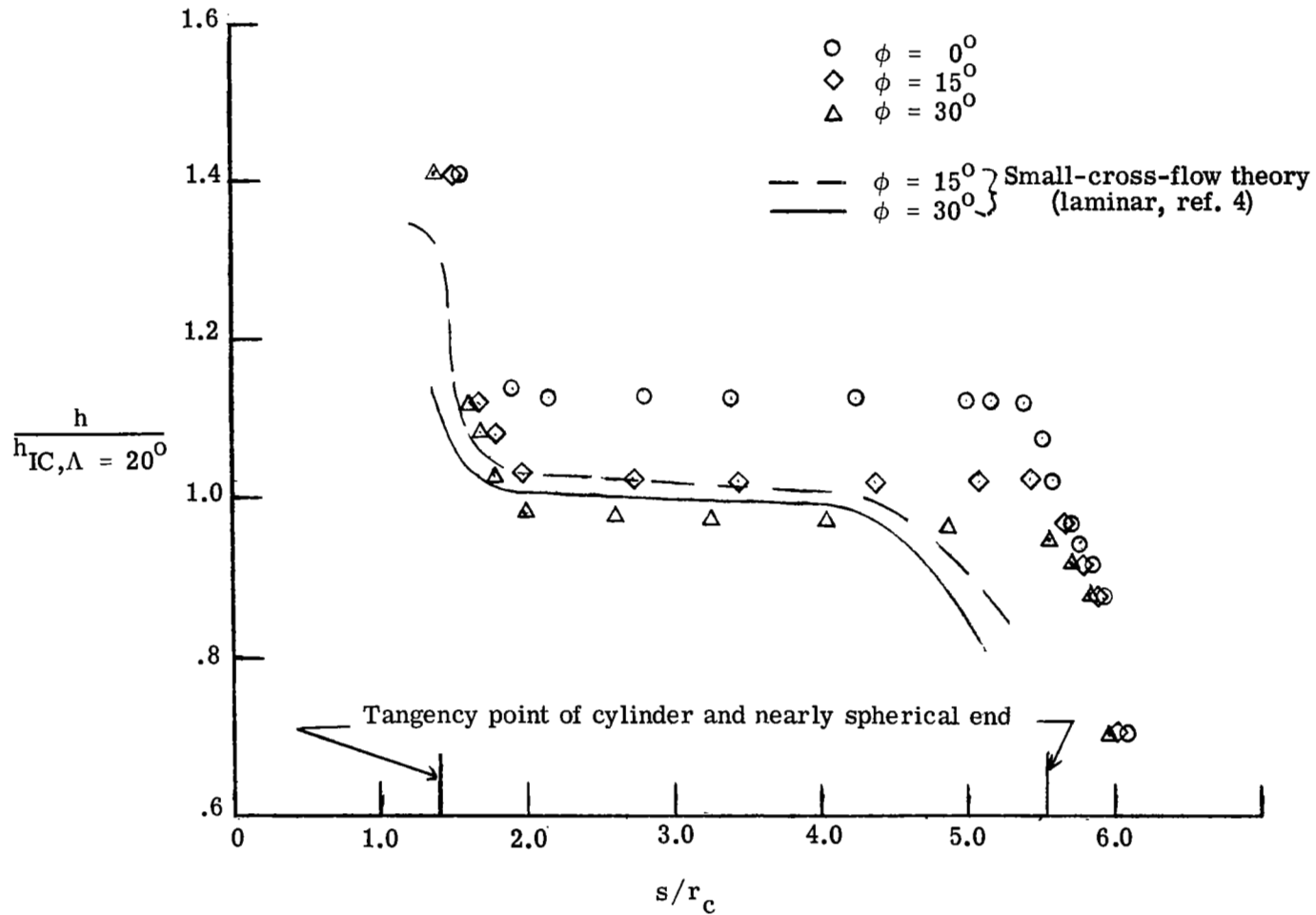
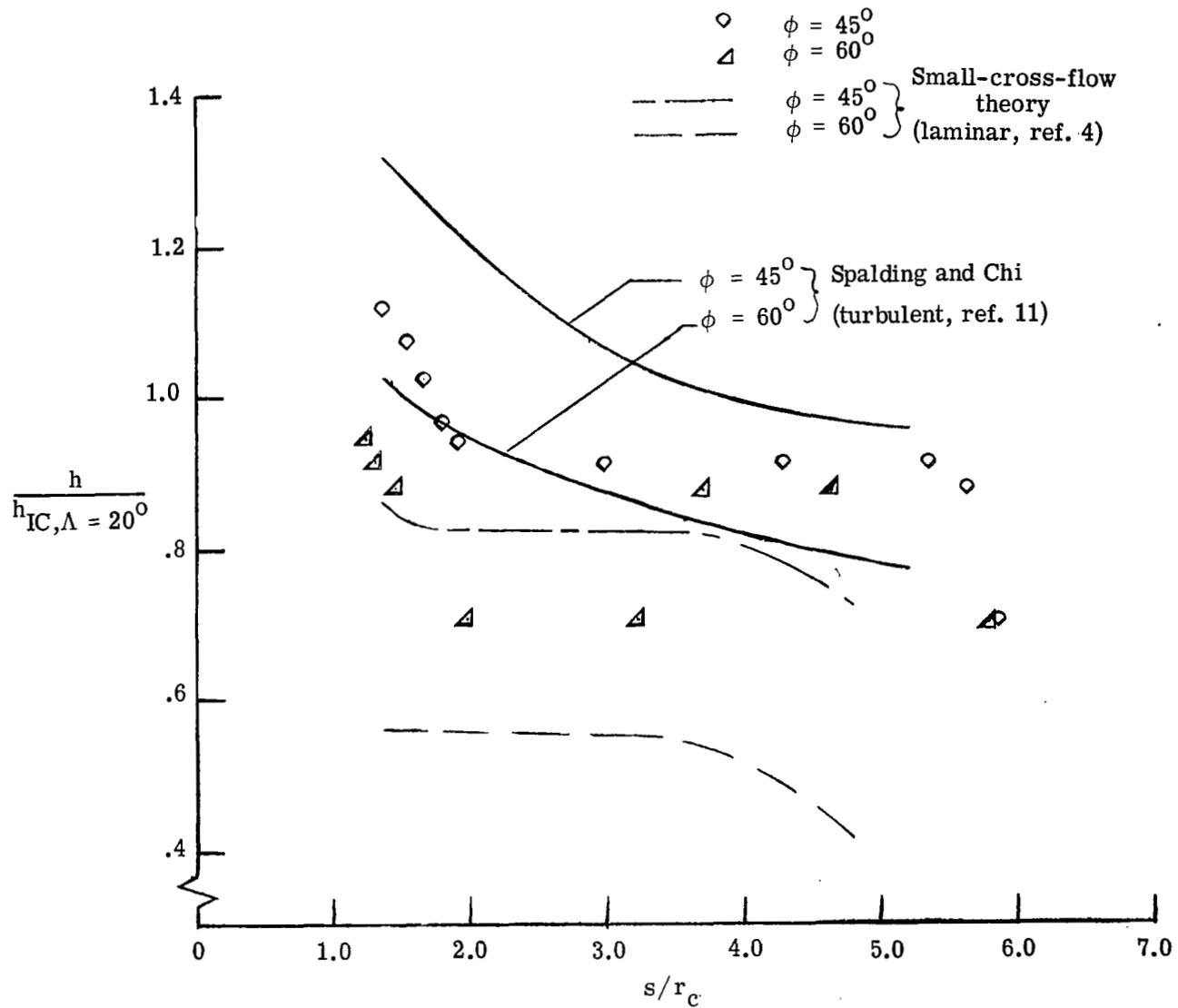


Figure 16.- Circumferential heat-transfer distribution for $\Lambda = 20^\circ$, $t = 0.72$, $R = 0.99 \times 10^6$, and $h_{1C, \Lambda=20^\circ} = 3.50 \times 10^2 \text{ W/m}^2\text{-}^\circ\text{K}$.
 Turbulent $h_{1C, \Lambda=20^\circ} = 6.54 \times 10^2 \text{ W/m}^2\text{-}^\circ\text{K}$.



(a) $\phi = 0^\circ$; $\phi = 15^\circ$; $\phi = 30^\circ$.

Figure 17.- Spanwise heat-transfer distribution for $\Lambda = 20^\circ$, $t = 0.72$, $R = 0.99 \times 10^6$, and $h_{IC, \Lambda = 20^\circ} = 3.5 \times 10^2 \text{ W/m}^2\text{-}^\circ\text{K}$.



(b) $\phi = 45^\circ$; $\phi = 60^\circ$.

Figure 17.- Concluded.

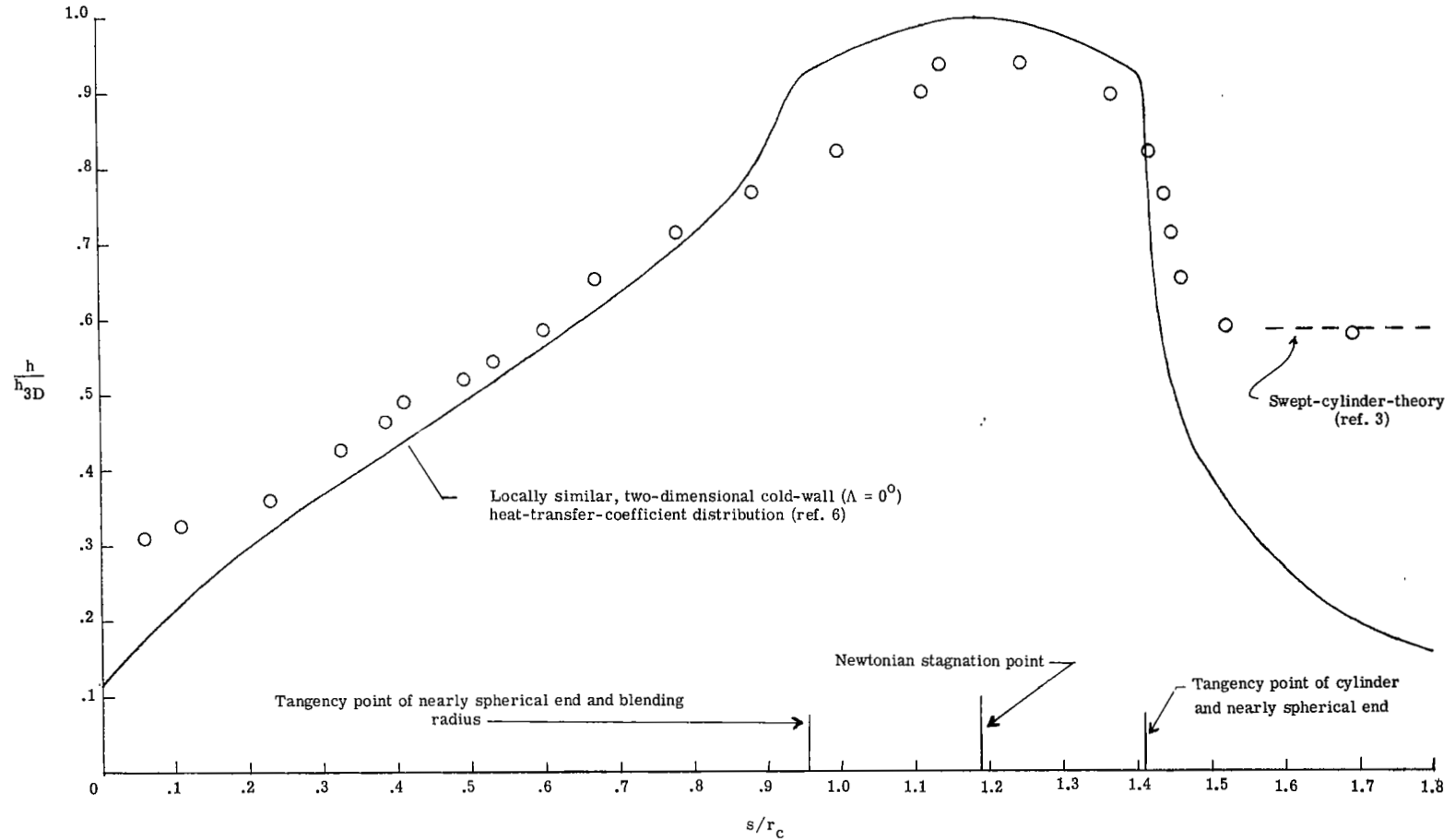
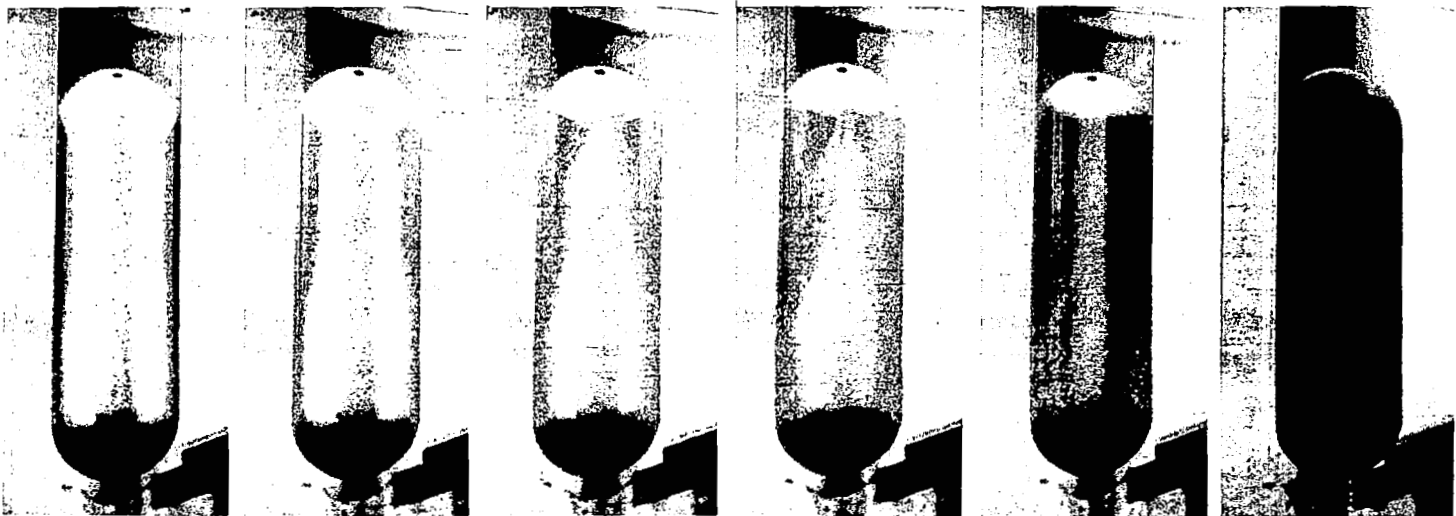


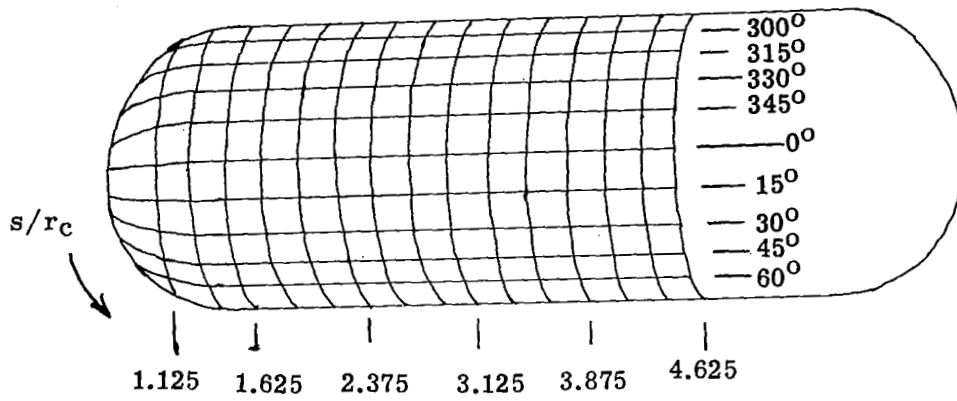
Figure 18.- Heat-transfer distribution along windward ray of nearly spherical end for $\Lambda = 20^\circ$, $t = 0.75$, $R = 0.97 \times 10^6$, and $h_{3D} = 5.94 \times 10^2 \text{ W/m}^2\text{-}^\circ\text{K}$.



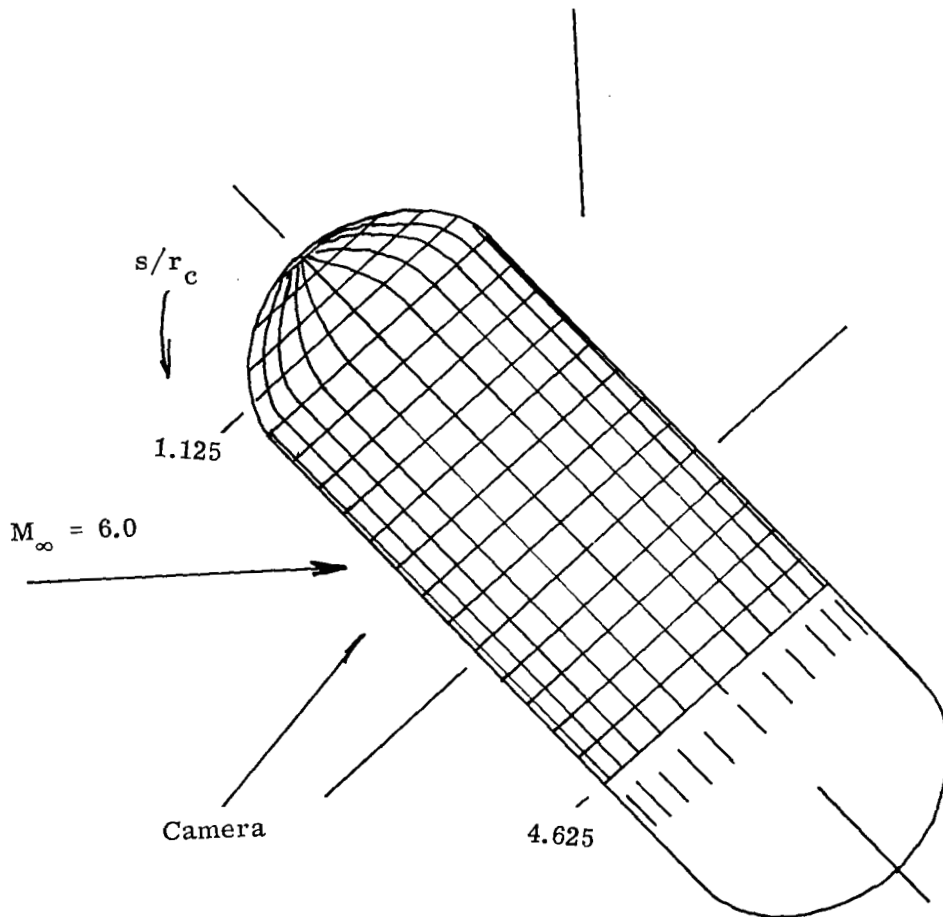
Increasing time



L-69-1322
Figure 19. - Photographs of phase-change patterns at $\lambda = 40^\circ$.



(a) Camera view.



(b) Profile view perpendicular to stream.

Figure 20.- Model orientation at $\Lambda = 40^\circ$.

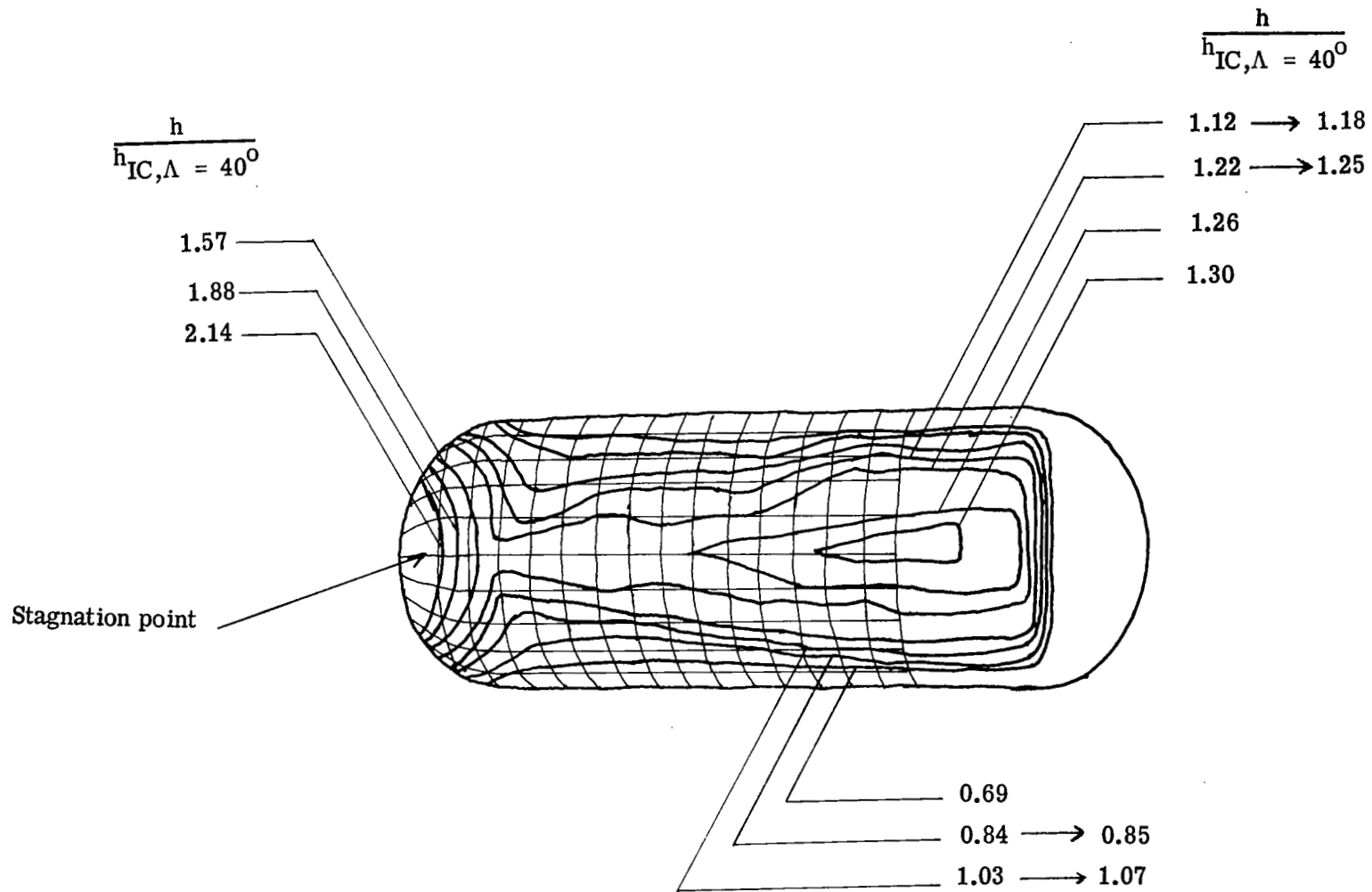


Figure 21.- Nominal heat-transfer-coefficient contours superimposed on camera view of grid model for $\Lambda = 40^\circ$, $t = 0.69$, $R = 0.96 \times 10^6$, and $h_{IC, \Lambda = 40^\circ} = 2.76 \times 10^2 \text{ W/m}^2\text{-}^\circ\text{K}$.

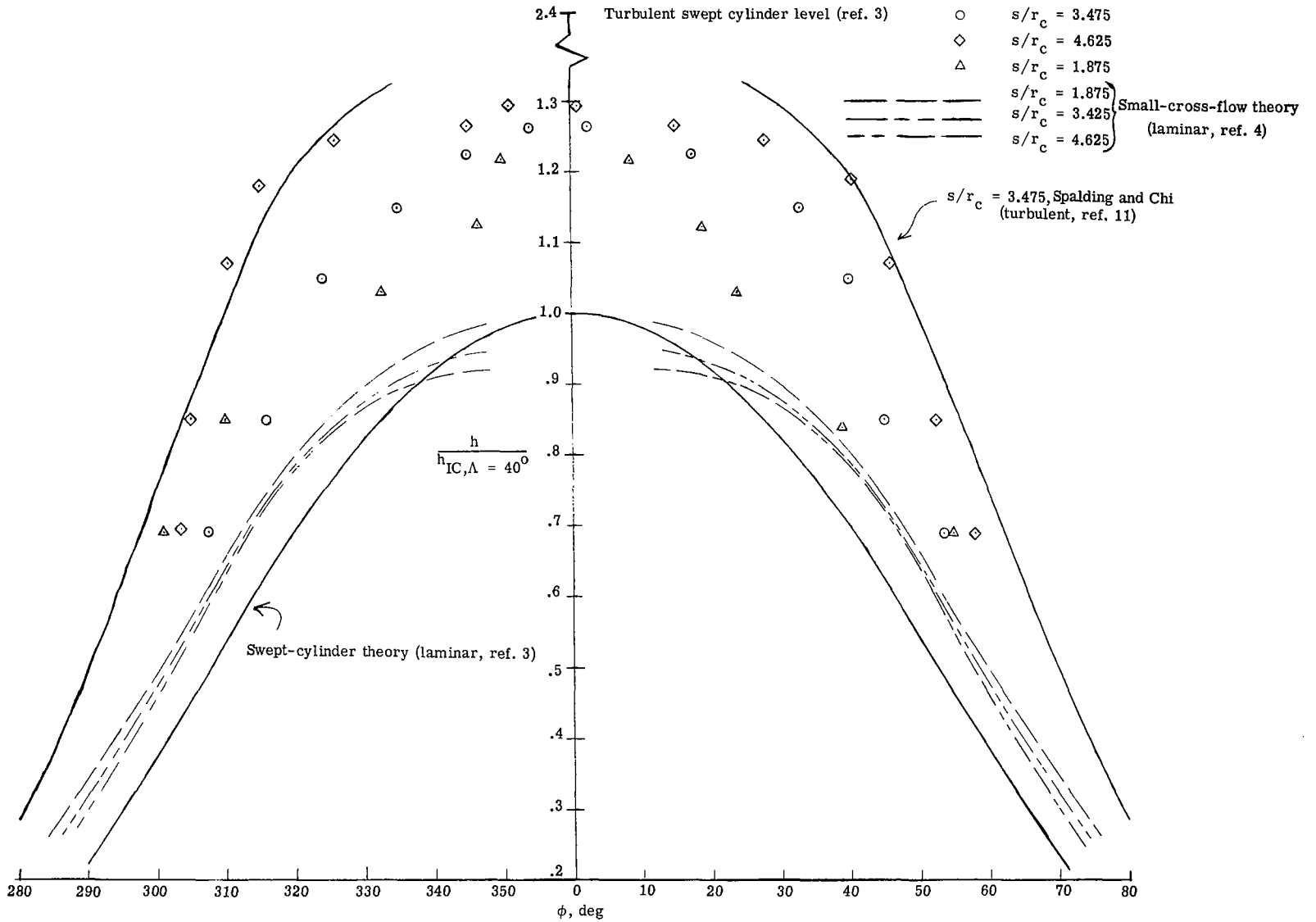
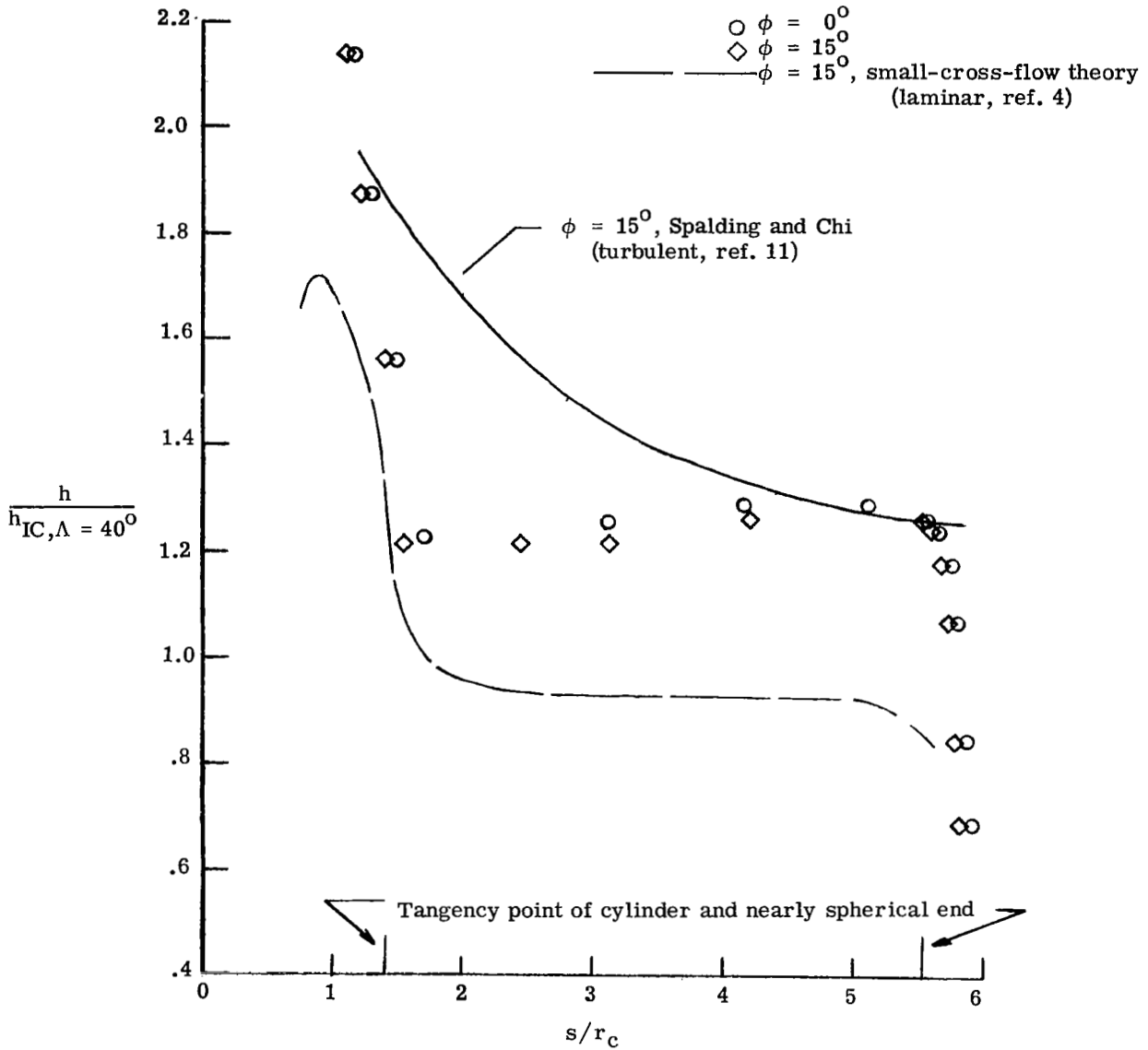
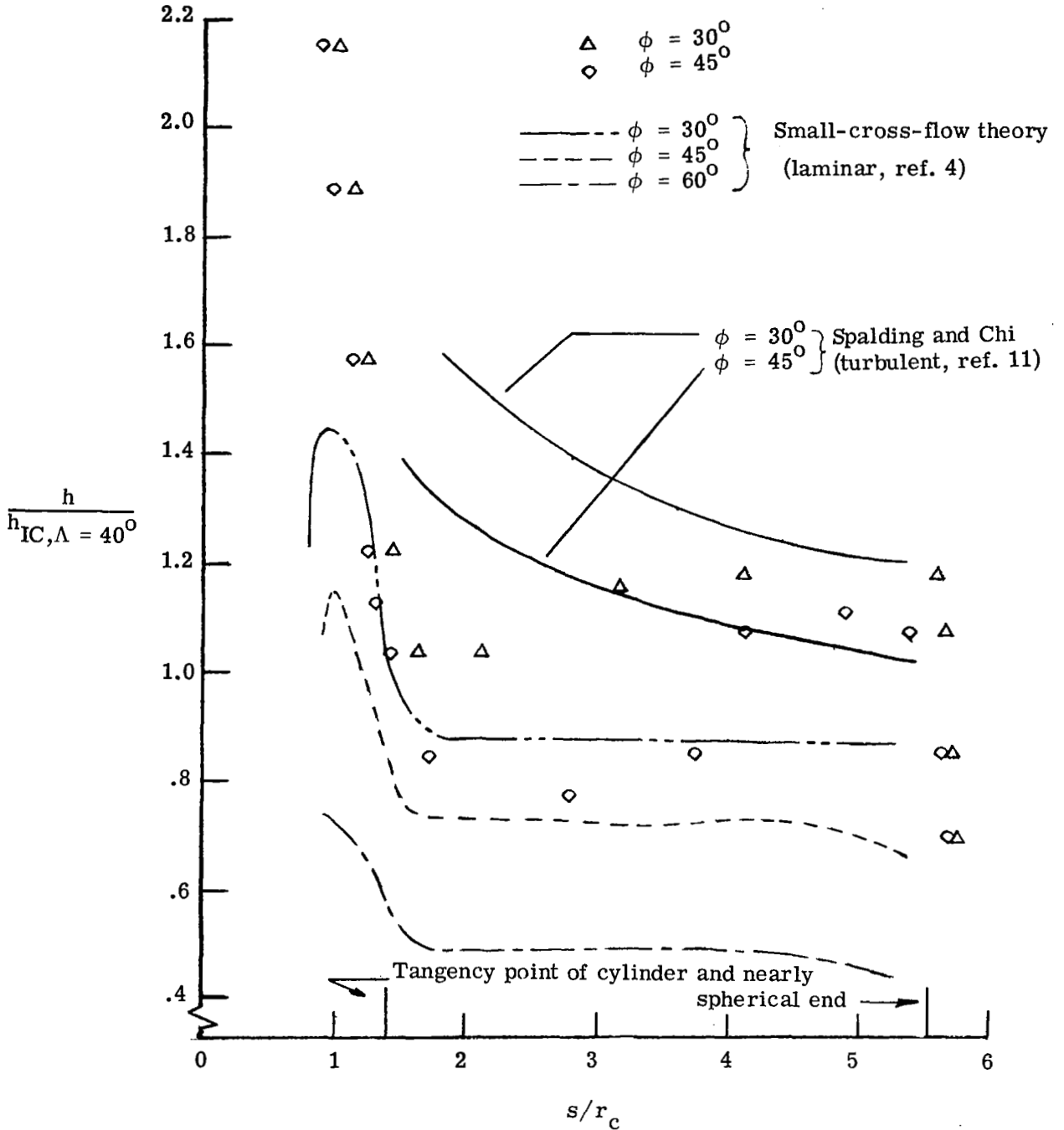


Figure 22.- Circumferential heat-transfer distribution for $\Lambda = 40^\circ$, $t = 0.69$, $R = 0.96 \times 10^6$, and $h_{IC, \Lambda = 40^\circ} = 2.76 \times 10^2 \text{ W/m}^2 \cdot 0\text{K}$.
 Turbulent $h_{IC, \Lambda = 40^\circ} = 6.66 \times 10^2 \text{ W/m}^2 \cdot 0\text{K}$.



(a) $\phi = 0^\circ$; $\phi = 15^\circ$.

Figure 23.- Spanwise heat-transfer distribution for $\Lambda = 40^\circ$, $t = 0.69$, $R = 0.96 \times 10^6$, and $h_{IC, \Lambda = 40^\circ} = 2.76 \times 10^2 \text{ W/m}^2\text{-}^\circ\text{K}$.



(b) $\phi = 30^\circ$; $\phi = 45^\circ$; $\phi = 60^\circ$.

Figure 23.- Concluded.